

253885-2-F (Vol. 1)

Final Report

UTILITY ANALYSIS OF HIGH-RESOLUTION MULTISPECTRAL IMAGERY

Volume 1: Performance Prediction Model (PPM) Assessment and
Magnetic Bearing System (MBS) Analysis and Modeling

G.L. Gerber, M.F. Reiley, and M.T. Eismann

Environmental Research Institute of Michigan
P.O. Box 134001
Ann Arbor, MI 48113-4001

J. M. Jacobs

J² and Associates
7800 Raintree Road
Centerville, OH 45459-5434

DISTRIBUTION STATEMENT A

Approved for public release
Distribution Unlimited

APRIL 1995

Sponsored by:

ASC/REFQ
2640 Loop Road West
Wright-Patterson AFB, OH 45433-7106

19960201 038

Contract No.: DLA900-88-D-0392
Delivery Order: 57

DTIC QUALITY INSPECTED 8

AD NUMBER		DATE	DTIC ACCESSION NOTICE	
1. REPORT IDENTIFYING INFORMATION			RE	
A. ORIGINATING AGENCY ERIM			1.	ss
B. REPORT TITLE AND/OR NUMBER Utility Analysis of High-Resolution Multispec Imagery. Vol. I Performance Prediction Model.			2.	2.
C. MONITOR REPORT NUMBER 253885-2-F (Vol. I)			4.	
D. PREPARED UNDER CONTRACT NUMBER DLA900-88-D-0392			5.	nt
2. DISTRIBUTION STATEMENT Unclassified/Unlimited				ir.

19960201 038

DTIC Form 50
DEC 91

PREVIOUS EDITIONS ARE OBSOLETE

ERIM-320		REPORT DOCUMENTATION PAGE		Form Approved OMB No. 0704-0188	
Public reporting burden for the collection of information is estimated to average 1 hour per response, including the time for reviewing instructions, searching existing data sources, gathering and maintaining the data needed, and completing and reviewing the collection of information. Send comments regarding this burden estimate or any other aspect of this collection of information, including suggestions for reducing this burden, to Washington Headquarters Services, Directorate for Information Operations and Reports, 1215 Jefferson Davis Highway, Suite 1204, Arlington, VA 22202-4302, and to the Office of Management and Budget, Paperwork Reduction Project (0704-0188), Washington, DC 20503.					
1. AGENCY USE ONLY (Leave Blank)		2. REPORT DATE April 1995		3. REPORT TYPE AND DATES COVERED Final 1/26/94 - 10/1/94	
4. TITLE AND SUBTITLE Utility Analysis of High Resolution Multispectral Imagery, Volume 1: Performance Prediction Model (PPM) Assessment and Magnetic Bearing System (MBS) Analysis and Modeling				5. FUNDING NUMBERS	
6. AUTHOR(S) G.L. Gerber, M.F. Reiley, J.M. Jacobs, and M.T. Eismann					
7. PERFORMING ORGANIZATION NAME(S) AND ADDRESS(ES) Environmental Research Institute of Michigan P.O. Box 134001 Ann Arbor, MI 48113-4001				8. PERFORMING ORGANIZATION REPORT NUMBER ERIM 253885-2-F (V1)	
9. SPONSORING/MONITORING AGENCY NAME(S) AND ADDRESS(ES) ASC/REFQ 2640 Loop Road West Wright-Patterson AFB, OH 45344-7106				10. SPONSORING/MONITORING AGENCY REPORT NUMBER	
11. SUPPLEMENTARY NOTES					
12a. DISTRIBUTION/AVAILABILITY STATEMENT				12b. DISTRIBUTION CODE	
13. ABSTRACT (Maximum 200 words) This report summarizes the results of two studies conducted to address specific issues related to the utility of a specific high-resolution multispectral sensor, designated the F sensor. The first study assessed the validity of a sensor model, entitled the Performance Prediction Model (PPM), which was provided by the sensor contractor. This was performed by cross-checking results with an independent sensor model. In most cases, good agreement was achieved. The second study assessed the expected performance of a vital component of the F sensor, a magnetic bearing system (MBS) for line-of-sight control and stabilization.					
14. SUBJECT TERMS Performance Modeling, E/O Sensor, Stabilization, Magnetic Bearing				15. NUMBER OF PAGES 49	
				16. PRICE CODE	
17. SECURITY CLASSIFICATION OF REPORT Unclassified		18. SECURITY CLASSIFICATION OF THIS PAGE Unclassified		19. SECURITY CLASSIFICATION OF ABSTRACT Unclassified	
				20. LIMITATION OF ABSTRACT UL	

PREFACE

This report documents a portion of the results of a study called "Utility Analysis of High-Resolution Multispectral Imagery" performed by the Electro-Optical Science Laboratory of the Environmental Research Institute of Michigan, Ann Arbor, Michigan, for the Air Force ASC/REFQ during the period January 1994 through May 1995. The work described was performed in part by J² and Associates, Centerville, OH. This study was performed under Delivery Order 57 within the Infrared Information Analysis Center (IRIA) program, contract number DLA900-88-D-0392, for which the Defense Electronic Supply Center (DESC), Dayton, Ohio, serves as the contracting agency. The ASC program manager was Doug Amlin. The ERIM program manager was Michael T. Eismann. The authors of this report are Garth Gerber, Michael Reiley, James M. Jacobs, and Michael T. Eismann.

CONTENTS

PREFACE	iii
FIGURES	vi
1.0 INTRODUCTION	1
2.0 PPM ASSESSMENT	3
2.1 OBJECTIVE	3
2.2 VISIBLE BAND, 160 KM METEOROLOGICAL RANGE COMPARISON	3
2.2.1 Signal-to-Noise Ratio	4
2.2.2 Modulation Transfer Function	4
2.2.3 Ground Resolved Distance	4
2.2.4 Image Quality	7
2.3 VISIBLE BAND, 23 KM METEOROLOGICAL RANGE COMPARISON	9
2.3.1 Signal-to-Noise Ratio	9
2.3.2 Modulation Transfer Function	9
2.3.3 Ground Resolved Distance	11
2.3.4 Image Quality	14
2.4 MID-WAVE INFRARED (MWIR) BAND, 23 KM METEOROLOGICAL RANGE	15
2.4.1 Signal-to-Noise Ratio	15
2.4.2 Modulation Transfer Function	15
2.4.3 Minimum Detectable Temperature Difference (MDT) and Ground Resolved Distance	17
2.5 SENSOR COVERAGE CONSIDERATIONS	17
2.6 SUMMARY	18
3.0 MBS STABILITY ANALYSIS AND MODELING	19
3.1 INTRODUCTION	19
3.2 LIST OF REFERENCE OR APPLICABLE DOCUMENTS	20
3.3 TECHNICAL DISCUSSION	21
3.4 CONCLUSION	24
4.0 REFERENCES	25
APPENDIX: MBS MATHCAD TEMPLATES	A-1

FIGURES

2-1	SNR Comparison for Visible Band, 160 km Met Range	5
2-2	Graphical Depiction of the Determination of f_{limit}	6
2-3	GRD Comparison for Visible Band, 160 km Met Range	7
2-4	IIRS vs. GRD from NATO Air Standard 101 IIRS Definitions	8
2-5	IIRS Comparison for Visible Band, 160 km Met Range	9
2-6	SNR versus Surface Range and Solar Zenith Angle, ESP Model, 23 km Met Range	10
2-7	SNR Comparison for Visible Band, 23 km Met Range	10
2-8	MTF Components for Visible Band, Nadir Viewing, ESP Model, 23 km Met Range	11
2-9	MTF Components for Visible Band, 200 km Range, ESP Model, 23 km Met Range	12
2-10	MTF Comparison for Visible Band, Nadir Viewing, 23 km Met Range	12
2-11	GRD for Selected Sun Angles, ESP Model, 23 km Met Range	13
2-12	GRD Comparison for Visible Band, 23 km Met Range	13
2-13	IIRS Predictions for Visible Band, 23 km Met Range	14
2-14	IIRS Comparison for Visible Band, 23 km Met Range	15
2-15	SNR Comparison for MWIR Band, 23 km Met Range	16
2-16	MTF Comparison for MWIR Band, 23 km Met Range	16
2-17	Coverage Swath Definitions	17
3-1	MBS Control Components	19
3-2	Free Body Diagram of MBS Structure	22
3-3	Actuator Control System Block Diagram	23
3-4	Actuator Control System Block Diagram	24

1.0 INTRODUCTION

This report summarizes the results of two studies conducted to address specific issues related to the utility of a specific high-resolution multispectral sensor, designated the F sensor. The first study assessed the validity of a sensor model, entitled the Performance Prediction Model (PPM), which was provided by the sensor contractor. This was performed by cross-checking results with an independent sensor model. In most cases, good agreement was achieved. The second study assessed the expected performance of a vital component of the F sensor, a magnetic bearing system (MBS) for line-of-sight control and stabilization.

The report is organized as follows. Section 2 provides the PPM assessment results. Section 3 overviews the MBS analysis. The appendix provides the details of the MBS modeling effort.

2.0 PPM ASSESSMENT

2.1 OBJECTIVE

The objective of this task was to perform an end-to-end comparison of sensor performance predictions made using the Performance Prediction Model (PPM), provided by the government [1], and the ERIM Sensor Performance (ESP) model. Since an exhaustive comparison of the two models was not desired, a "black box" approach was utilized which (for identical model inputs) compared PPM and ESP model output predictions for two key sensor performance prediction metrics:

- 1) Ground Resolved Distance (GRD);
- 2) an image quality metric based on the Image Interpreter Rating Scale (IIRS) [2].

Several internal (to the "black box") checks were also made for key intermediate results:

- 1) Signal-to-noise-ratio (SNR);
- 2) System Modulation Transfer Function (MTF).

The PPM was developed to model the F sensor. Approximately 200 sensor parameters were supplied which define this sensor and are used within the PPM to predict the sensor performance. Rather than attempt to replicate the level of detail within the PPM (a "bottom-up" approach), the ESP "top-down" modeling approach started with the most significant parameters which affect sensor performance prediction and added detail only if the performance predictions were significantly affected. The ESP model had been used to predict performance metrics for the F sensor as part of an prior modeling effort, using input data provided by the F sensor contractor. The input data currently used by the PPM varied slightly from that provided (or assumed) for the prior study. In accordance with the "black box" approach, the following input data was taken from the PPM and input to the ESP model:

Optical MTF
Optical transmission
Detector MTF
Detector responsivity

Comparison of modeling results obtained from the ESP and PPM models for the visible band will be presented first, followed by a comparison of modeling results for the medium wave IR band.

2.2 VISIBLE BAND, 160 KM METEOROLOGICAL RANGE COMPARISON

The PPM contains a very high visibility sensor viewing scenario (called a "Case") with the following pertinent parameters:

160 km meteorological range
 14 degree solar zenith angle
 No atmospheric turbulence
 20 km sensor altitude, 200 m/s velocity

Comparisons between the PPM and ESP models for the 160 km case were performed for SNR, MTF, GRD, and IIRS. The following paragraphs briefly describe the results of the comparisons.

2.2.1 Signal-to-Noise Ratio

The ESP model was run for the above 160 km met range case (using MODTRAN) and the signal-to-noise calculated at 16 different surface (standoff) ranges. Here, signal (or contrast signal) is defined as the difference signal obtained between a detector element fully illuminated with a 15% target reflectance and a detector element fully illuminated with 7% background reflectance. The PPM was run for the same viewing scenario at 0, 100 and 200 km surface range. Each surface range calculation required approximately 5 minutes of computing time, prohibiting running the PPM at all of the ranges. The resulting per pixel SNR values are graphed in Figure 2-1 and compare very well, indicating that (in spite of the different implementation details) consistent SNR results are obtained. This result indicates that basic sensor model components (e.g. aperture area, detector responsivity, wavelength region) and scene radiance (determined from LOWTRAN or MODTRAN) correspond closely between the two models.

2.2.2 Modulation Transfer Function

See the following 23 km meteorological range visibility for MTF comparison discussion and plots.

2.2.3 Ground Resolved Distance

The ground resolved distance (GRD) calculation predicts the ground distance for any given slant range, SR, corresponding to one cycle of the standard Air Force Tri-bar target predicted to be at the visual detection limit. GRD is calculated as follows:

$$GRD = \frac{SR}{f_{limit}} \quad (2-1)$$

where f_{limit} is the limiting spatial frequency, determined by the spatial frequency at which

$$MTF(f_{limit}) \cdot SNR(SR) \cdot \frac{f_{Nyquist}}{f_{limit}} = SNRD = 3 \quad (2-2)$$

or

$$f_{\text{limit}} = f_{\text{Nyquist}} \quad (2-3)$$

whichever is less. SNRD is a detection threshold SNR determined empirically to be 3 for the visual task of just resolving the tri-bar target. The ratio of the limiting frequency to the Nyquist frequency is a SNR-weighting term which accounts for the fact that the eye spatially averages the noise over the larger bars, effectively improving the signal-to-noise at lower spatial frequencies (more pixels per bar). The limiting spatial frequency is not permitted to exceed the Nyquist frequency (i.e. is bounded above) due to the confounding effects of aliasing on the visual system. The GRD metric combines both MTF and SNR characteristics of a sensor and is an indicator of image quality.

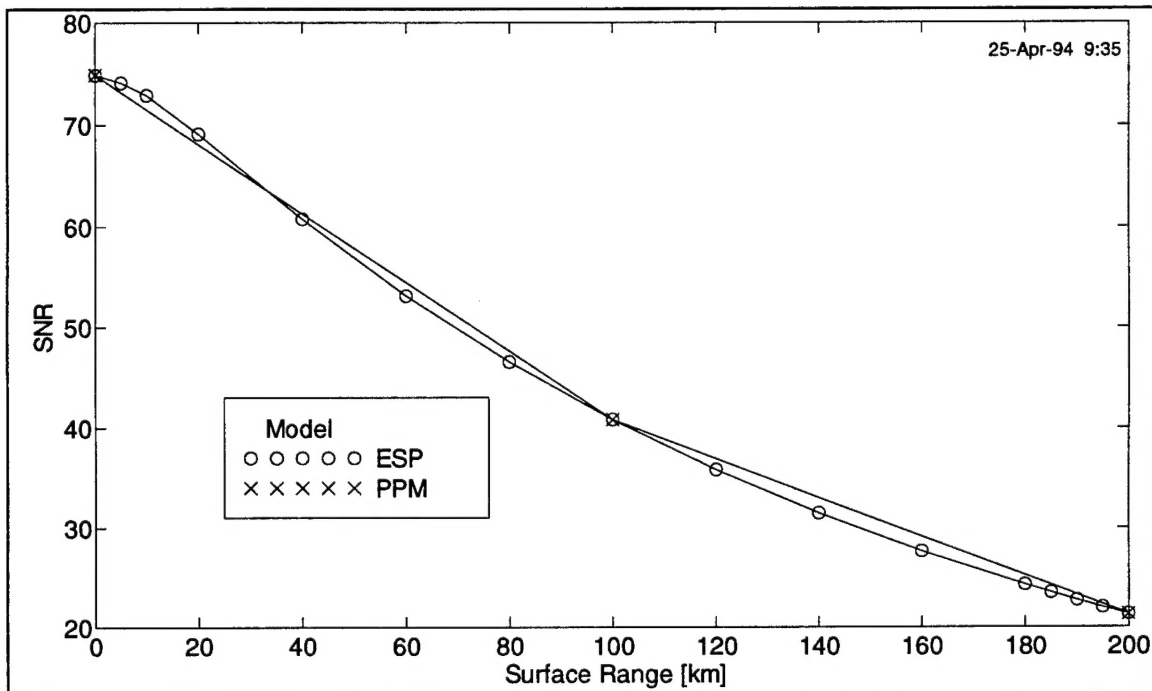
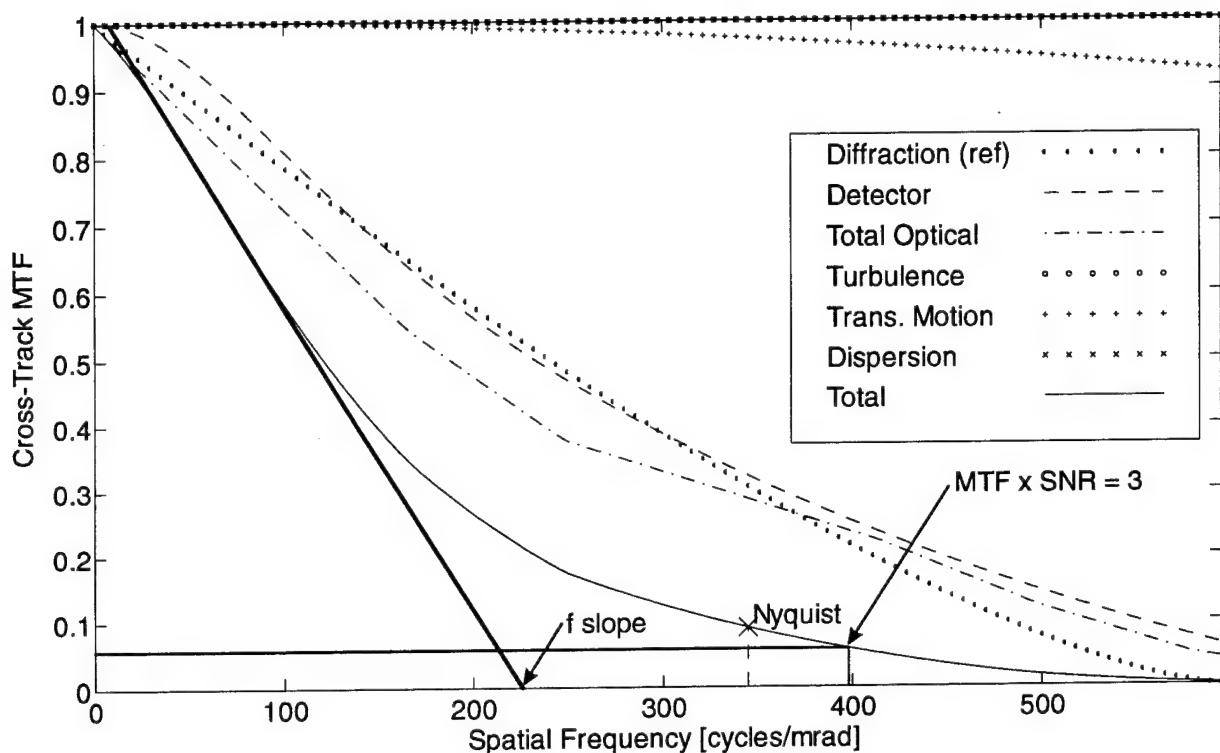


Figure 2-1: SNR Comparison for Visible Band, 160 km Met Range

For this study, the ESP model incorporated an IIRS prediction equation which includes the above conventional prediction of the GRD, but with an additional constraint placed on f_{limit} which applies in cases of high signal-to-noise when the optical MTF limits the bandwidth of the sensor (as opposed to the detector MTF or Nyquist condition limiting f_{limit}). This constraint does not permit f_{limit} to increase to unduly large values as SNR increases (e.g. due to a long, high spatial-frequency tail in the MTF), but recognizes that the system MTF introduces a limiting spatial frequency for conditions of high SNR. The method adopted to protect against unduly small GRD due to a long "tail" in the MTF (with little area under the curve)

approximates an effective bandwidth for the system by the following (heuristic) technique, illustrated in Figure 2-2.

- 1) The inflection point of the system MTF curve was found.
- 2) A tangent to the curve at that point was constructed.
- 3) The intersection of that curve and the spatial frequency axis, f_{slope} , was found.
- 4) This value was used in the calculation of GRD if it was less than the Nyquist



frequency and the limiting frequency determined from the product of the MTF and SNR (described above).

Figure 2-2: Graphical Depiction of the Determination of f_{limit}

The Nyquist limit also protects against a long MTF tail, but the above procedure provides protection for those cases where the optics (or LOS jitter) are limiting the system MTF and a long system MTF tail (with little associated area) is present.

GRD was calculated for the same set of surface ranges for the two models. The results are shown in Figure 2-3. The PPM model indicates consistently smaller GRD than the ESP. The source of the difference is due to the modified GRD definition used in the ESP (i.e. the f_{slope} term was less than Nyquist or the limiting frequency determined from the product of the MTF and SNR in this case). As can be seen in Figure 2-2, a fairly large area is present under the MTF

curve beyond the f_{slope} point (in this particular case). A better way to determine an equivalent bandwidth would be to adjust f_{slope} until the area in the triangular region is equal to the area under the system MTF curve. This limiting frequency would be insensitive to long MTF tails with little associated area, but would not be as "heavy handed" as the current procedure.

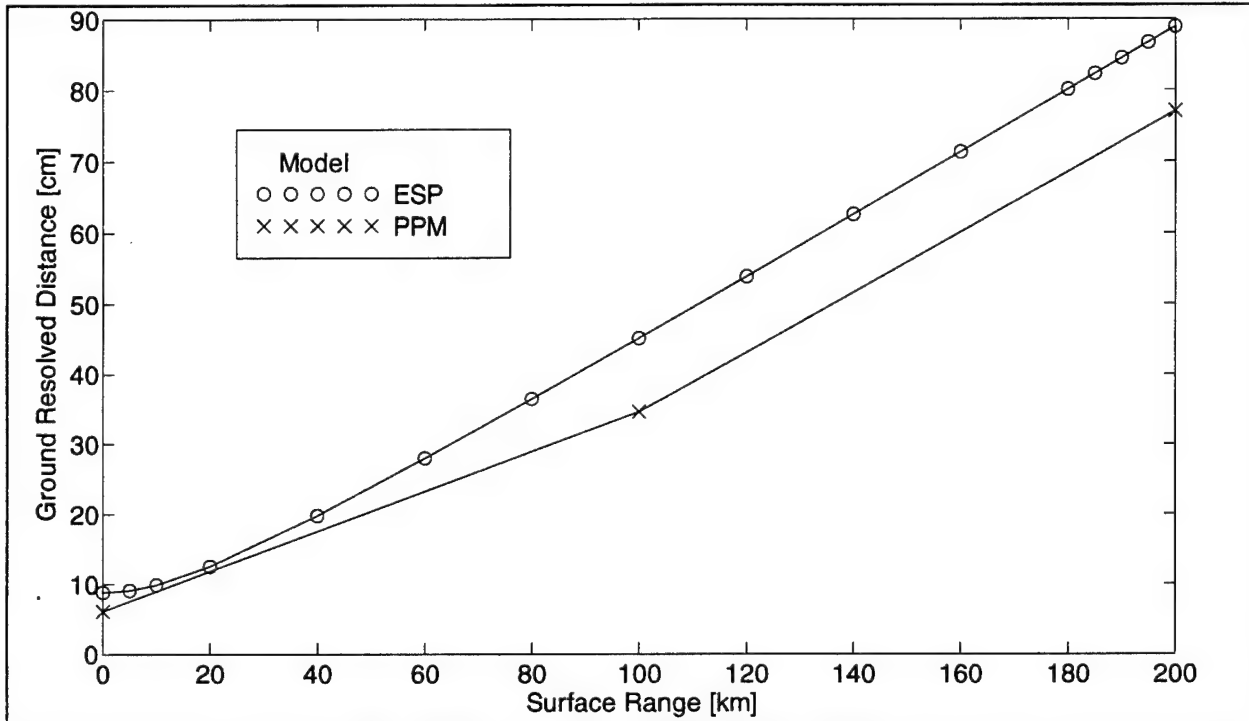


Figure 2-3: GRD Comparison for Visible Band, 160 km Met Range

2.2.4 Image Quality

For this study, the ESP model calculated IIRS using the following equation:

$$IIRS = 11.6 - 3.6 \cdot \log\left(\frac{GRD}{2}\right) \quad (2-4)$$

where GRD (in cm) was calculated as described above. The slope and intercept were determined by plotting the GRD values for the IIRS categories provided in the NATO Air Standard 101 Document (Reference 1) as shown in Figure 2-4.

The PPM model calculates IIRS using an image quality equation (IQE) of the following form:

$$IIRS = a_1 + a_2 \cdot \log(RER) - a_3 \cdot H - a_4 \cdot \log(GSD) - \frac{a_5}{SNR} \quad (2-5)$$

where RER is the relative edge response, GSD is the ground sampled distance, and H is an edge overshoot correction term. The RER is a number between 0 and 1 equal to the measured change in contrast between two pixels centered on a unit step in input contrast. It is proportional to the area under the system MTF curve. Better optical systems (with wider bandwidth) will have RER values closer to unity. For a sensor with RER close to unity and large SNR, image quality will be determined by the ground sampled distance (GSD) which is dependent only on detector pitch and effective focal length of the optical system. See the PPM documentation (Reference 2) for precise definitions of the RER and H terms. Values (from the PPM) used for the coefficients were $a_1 = 11.8$; $a_2 = 2.71, 3.32$; $a_3 = 1.48$; $a_4 = 3.45, 3.32$, $a_5 = 0.39$. Coefficients a_2 and a_4 vary for the along-track and cross-track case.

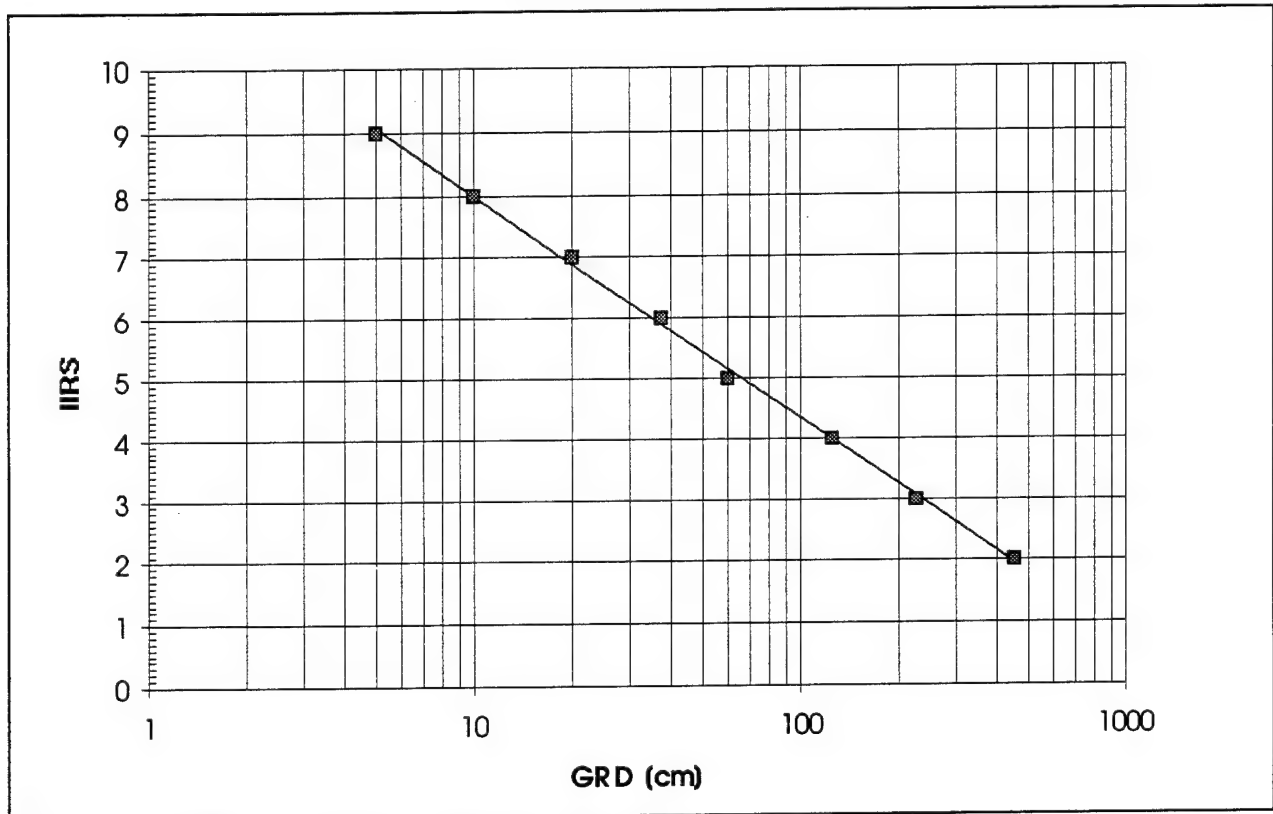


Figure 2-4: IIRS vs. GRD from NATO Air Standard 101 IIRS Definitions

IIRS image quality was predicted using the PPM IQE equation and the ESP equation based on GRD. The results are plotted in Figure 2-5. The agreement is within 0.2 IIRS at nadir and 0.4 IIRS at 200 km surface range, a remarkable agreement, given the different approach used to calculate IIRS in the two models. Consistent with the extremely good visibility, the dashed ESP IIRS line indicates that image quality is limited primarily by the system MTF (signal-to-noise is more than adequate) and Nyquist-limiting has not yet been reached (i.e. f_{slope} was used to calculate GRD).

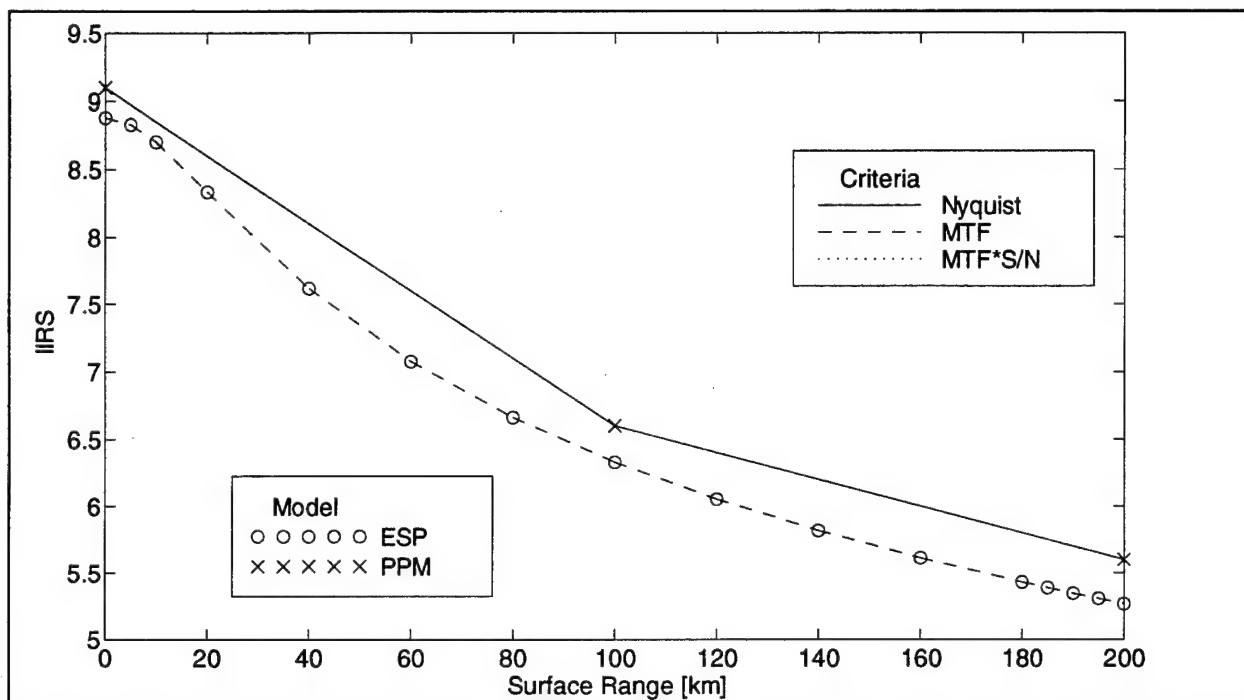


Figure 2-5: IIRS Comparison for Visible Band, 160 km Met Range

2.3 VISIBLE BAND, 23 KM METEOROLOGICAL RANGE COMPARISON

Model performance prediction comparisons were made for the visible band at the more realistic high-visibility condition of 23 km meteorological range, 74 degree solar zenith angle, and nominal turbulence ($R_0 = 0.8$ m). Note that northern hemisphere mid-latitude solar zenith angle is not less than 60 degrees even at mid-day during winter months.

2.3.1 Signal-to-Noise Ratio

The ESP model was used to calculate SNR for various solar zenith angles and surface ranges. The results are shown in Figure 2-6. SNR values were calculated using the PPM at 74 degrees solar zenith angle. The results are plotted in Figure 2-7. Again, the results compare well, given slight differences in model implementation.

2.3.2 Modulation Transfer Function

System MTF contributors for a nadir viewing sensor, as modeled using the ESP model, are shown in Figure 2-8. The system MTF is determined primarily by the optical and detector MTF characteristics of the sensor. Smear due to the sweep motion of the whiskbroom in the cross-track direction is greatly reduced due to the 4-phase clocking used with the TDI detector (effectively permitting charge transfer in $\frac{1}{2}$ IFOV increments). The sensor will exhibit some

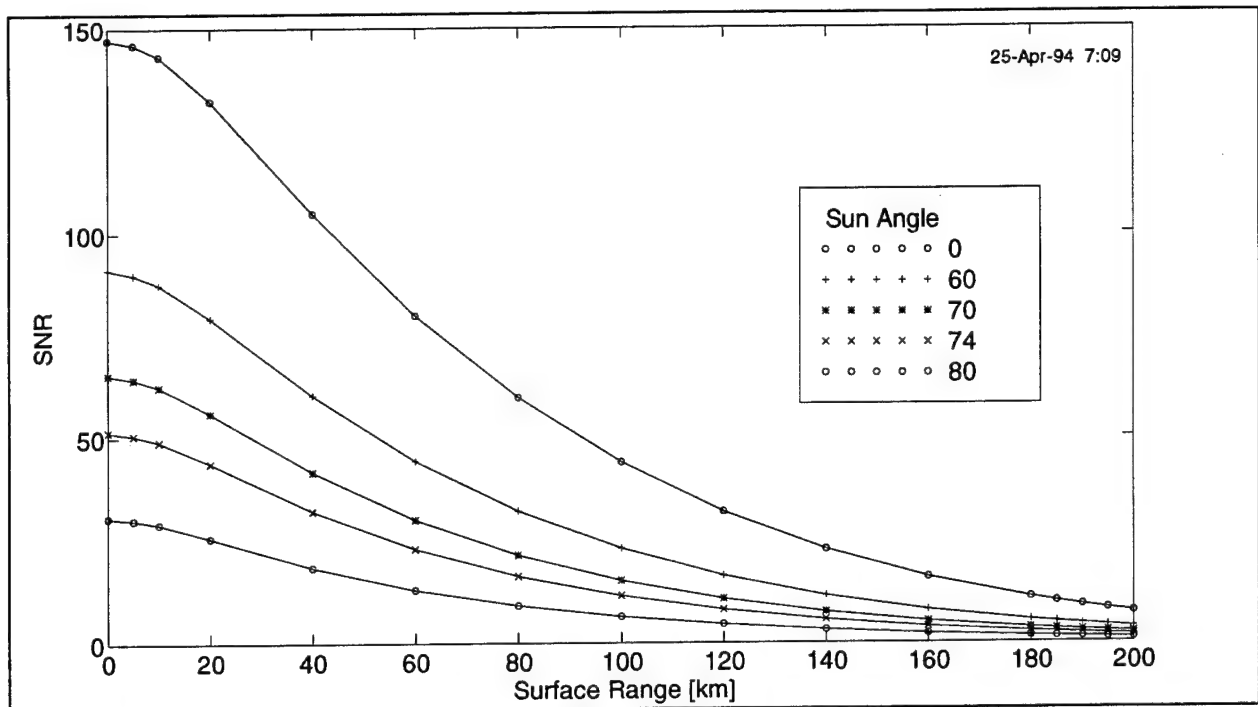


Figure 2-6: SNR versus Surface Range and Solar Zenith Angle, ESP Model, 23 km Met Range

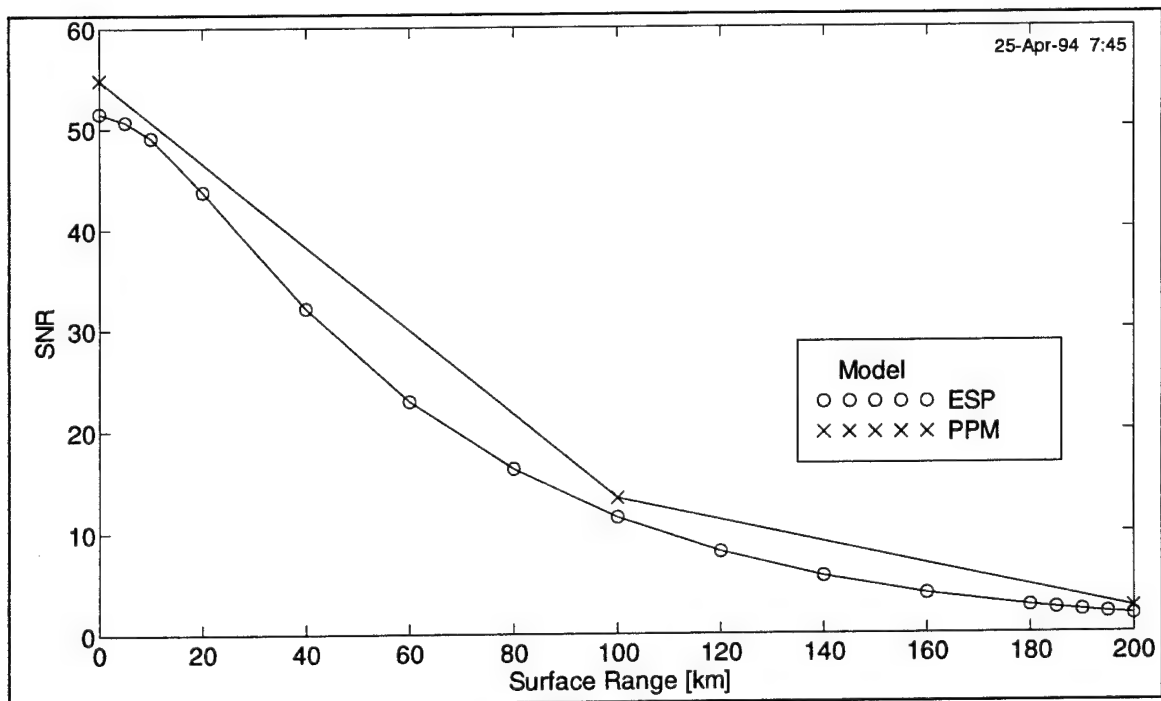


Figure 2-7: SNR Comparison for Visible Band, 23 km Met Range

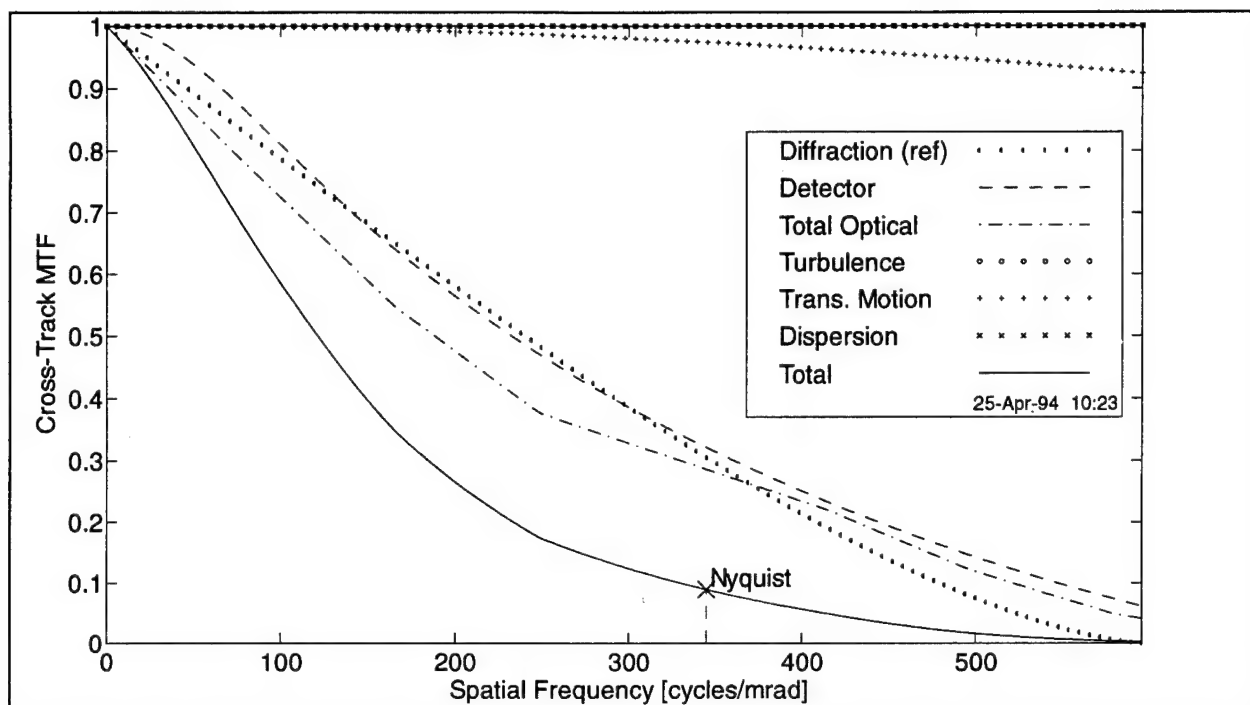


Figure 2-8: MTF Components for Visible Band, Nadir Viewing, ESP model, 23 km Met Range

aliasing, as indicated by the Nyquist frequency. Line-of-sight (LOS) jitter was assumed (by the PPM) to be negligible. The ESP model did not include jitter to permit direct comparison with the PPM results. The MTF contributors at 200 km surface range are shown in Figure 2-9. Since the whiskbroom angular scan rate is constant, there is no increase in blue due to a longer integration time at longer ranges (as would be observed with a pushbroom sensor). The system MTF calculated using each model is shown in Figure 2-10 for comparison. The PPM system MTF is lower than the ESP curve due to a boundary layer MTF degradation, not included in the ESP modeling. This degradation is modeled (in the PPM) as a constant (with spatial frequency) 0.86.

2.3.3 Ground Resolved Distance

Predicted GRD values (cm) for varying surface range and solar zenith angles were computed using the ESP model. The results are shown in Figure 2-11. Up to 80 km surface range, the GRD is dominated by the system MTF and is insensitive to the solar illumination level. A comparison of the predicted GRD for the ESP and PPM models is shown in Figure 2-12. The GRD agreement is better than might be expected since the MTF and SNR differences between the models compensate in the GRD calculation.

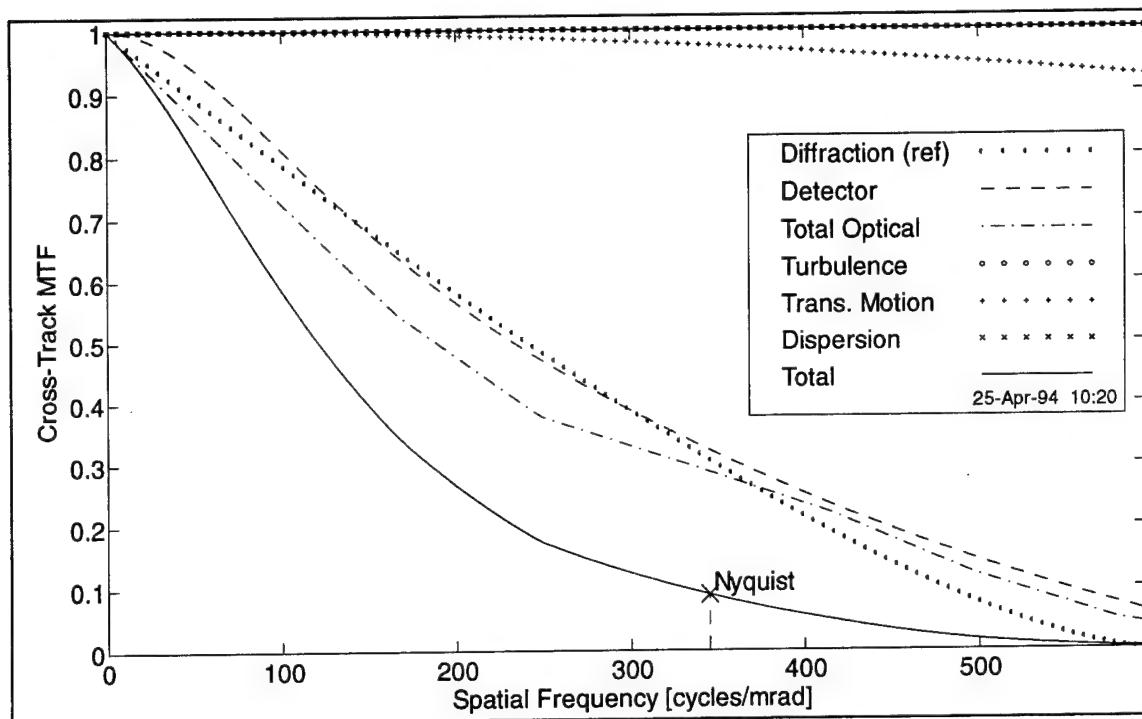


Figure 2-9: MTF Components for Visible Band, 200 km Range, ESP Model, 23 km Met Range

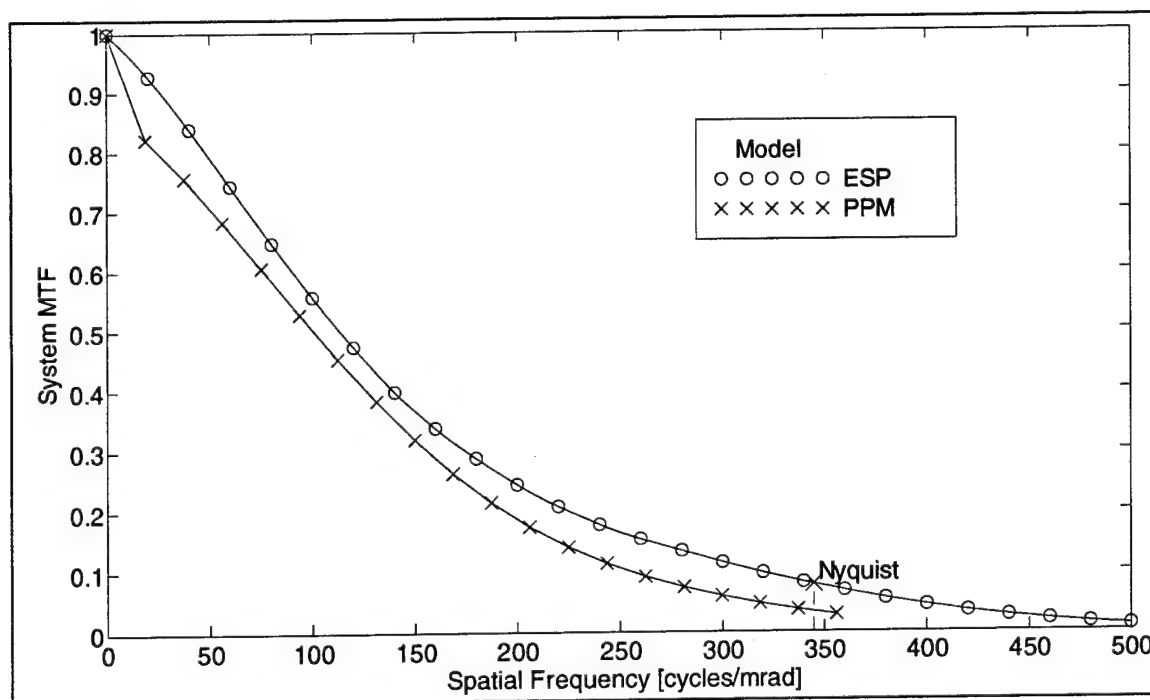


Figure 2-10: MTF Comparison for Visible Band, Nadir Viewing, 23 km Met Range

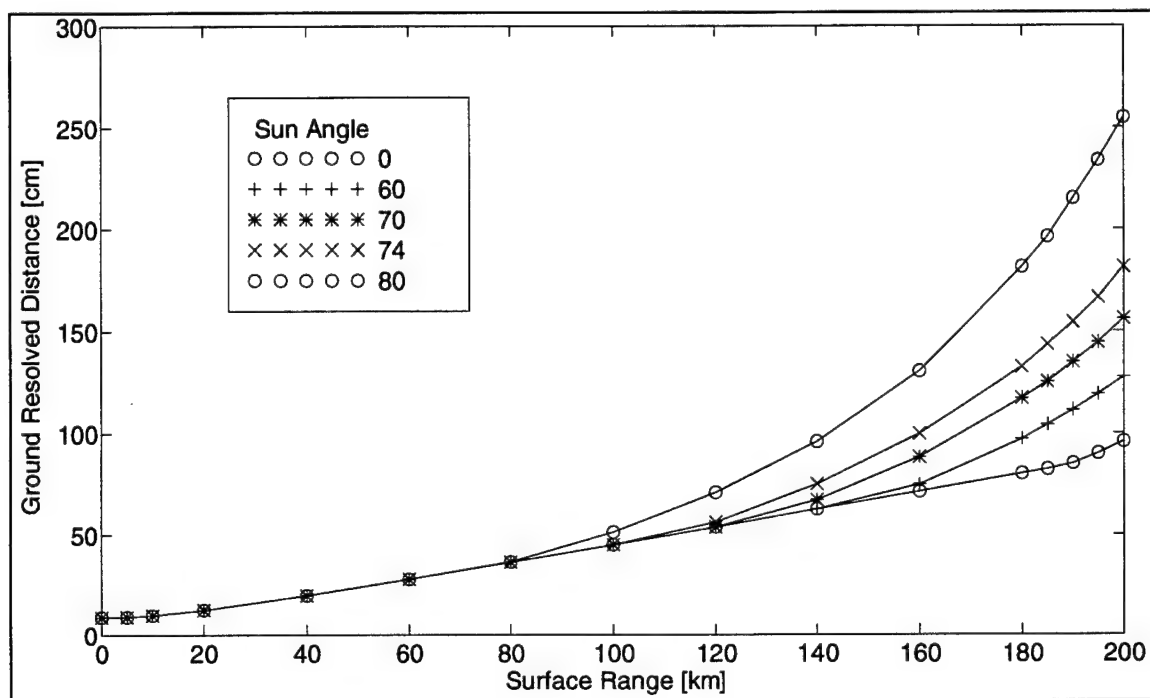


Figure 2-11: GRD for Selected Sun Angles, ESP Model, 23 km Met Range

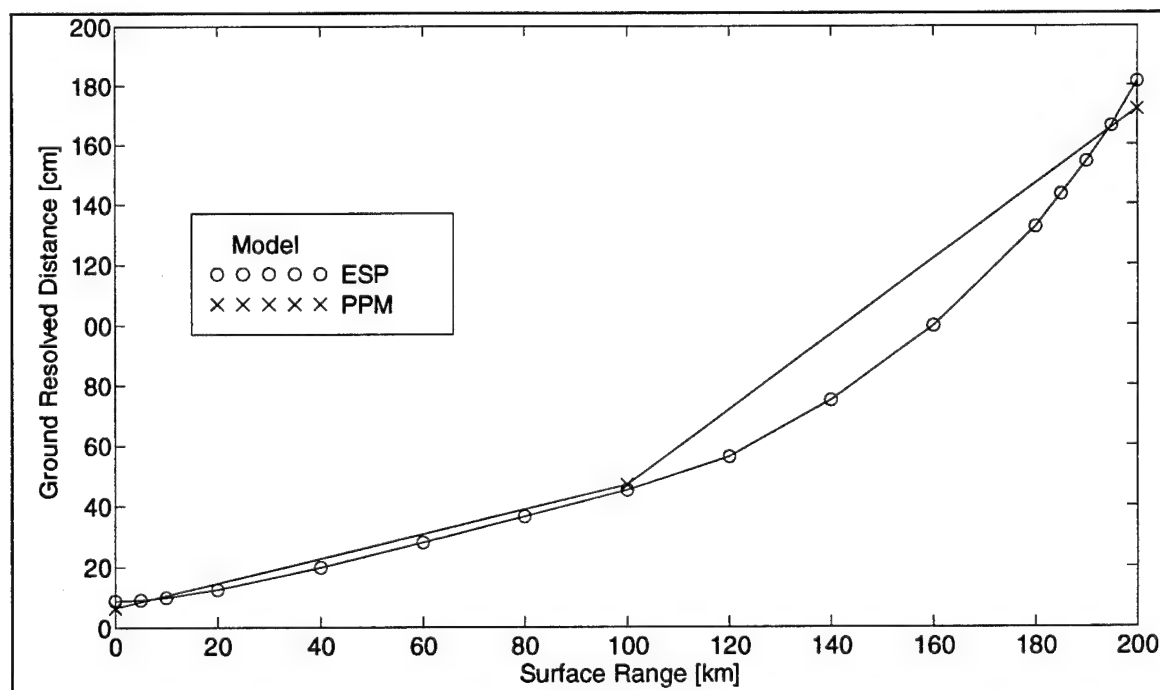


Figure 2-12: GRD Comparison for Visible Band, 23 km Met Range

2.3.4 Image Quality

Predicted IIRS using the ESP model are shown in Figure 2-13. At low solar zenith angles the SNR does not play a significant role in determining IIRS (MTF dominates). At longer surface ranges and higher zenith angles, the product of the system MTF and SNR plays a significant role (through the GRD calculation). The curve type indicates the dominating IIRS contributor.

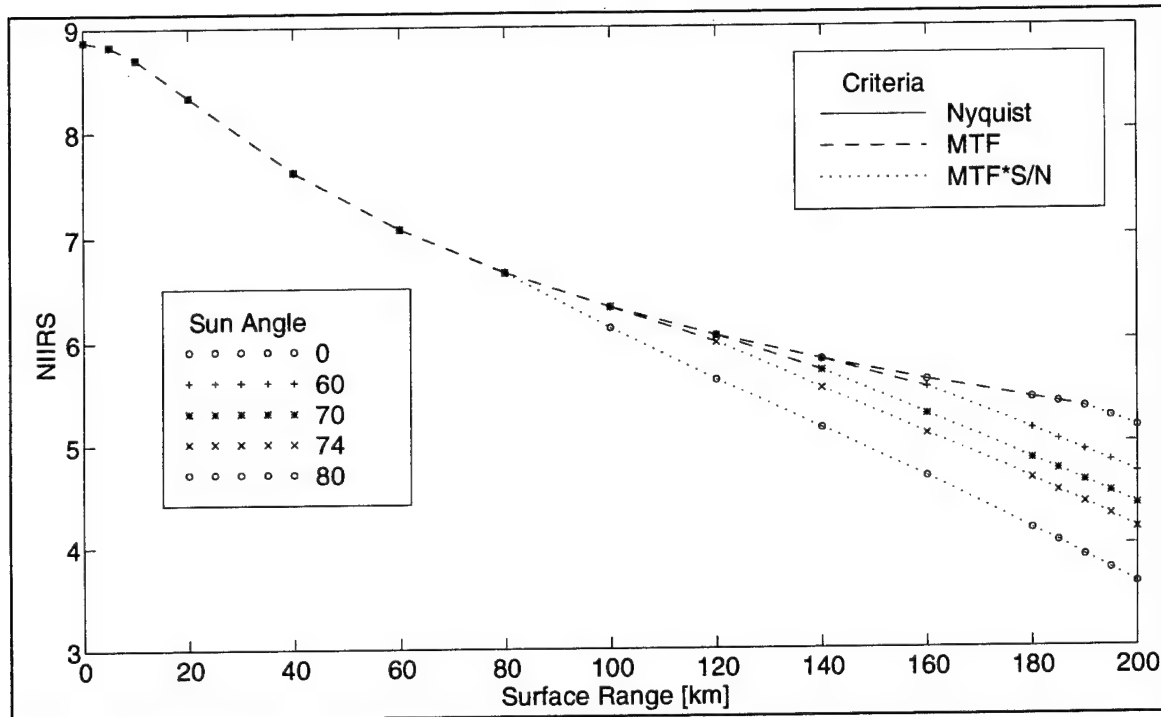


Figure 2-13: IIRS Predictions for Visible Band, 23 km Met Range

IIRS image quality was predicted using the PPM IQE equation and the ESP equation (based on GRD). The results are plotted in Figure 2-14. The agreement is within 0.2 IIRS at nadir (as with the 160 km met range case). At 200 km surface range, the ESP model indicates considerable degradation due to the decrease in SNR (and associated increase in GRD). The PPM results are very similar to the 160 km met range case, since the very small coefficient used in the IQE equation in the PPM model assigns little weight to SNR. Since the PPM predictions for GRD indicate an 2.25 factor increase at 200 km relative to the 160 km met range result, the PPM coefficient for the SNR term is questionable as is the IIRS prediction at longer ranges (or lower SNR). For every factor of 2 increase in GRD, IIRS is expected to decrease by one.

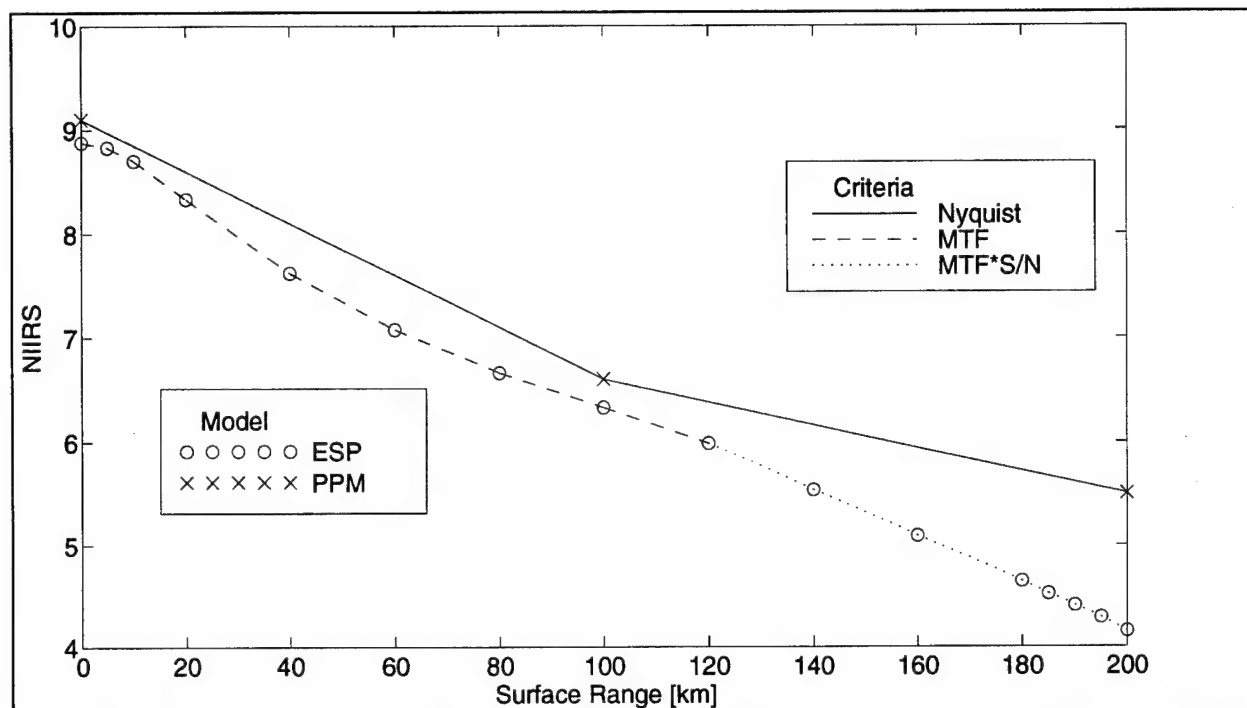


Figure 2-14: IIRS Comparison for Visible Band, 23 km Met Range

2.4 MID-WAVE INFRARED (MWIR) BAND, 23 KM METEOROLOGICAL RANGE COMPARISON

A comparison of the PPM and ESP models was also performed for the MWIR band. Signal-to-noise, and MTF calculations were performed with both models and the results compared.

2.4.1 Signal-to-Noise Ratio

Signal-to-noise calculations for the MWIR band using the two models are shown in Figure 2-15. As in the visible band, the results indicate that the conversion of scene radiance to detected signal yields consistent values across the two models.

2.4.2 Modulation Transfer Function

Comparison of the system MTF curves calculated using the two models also indicate very similar results as shown in Figure 2-16. The MWIR band will also exhibit some aliasing.

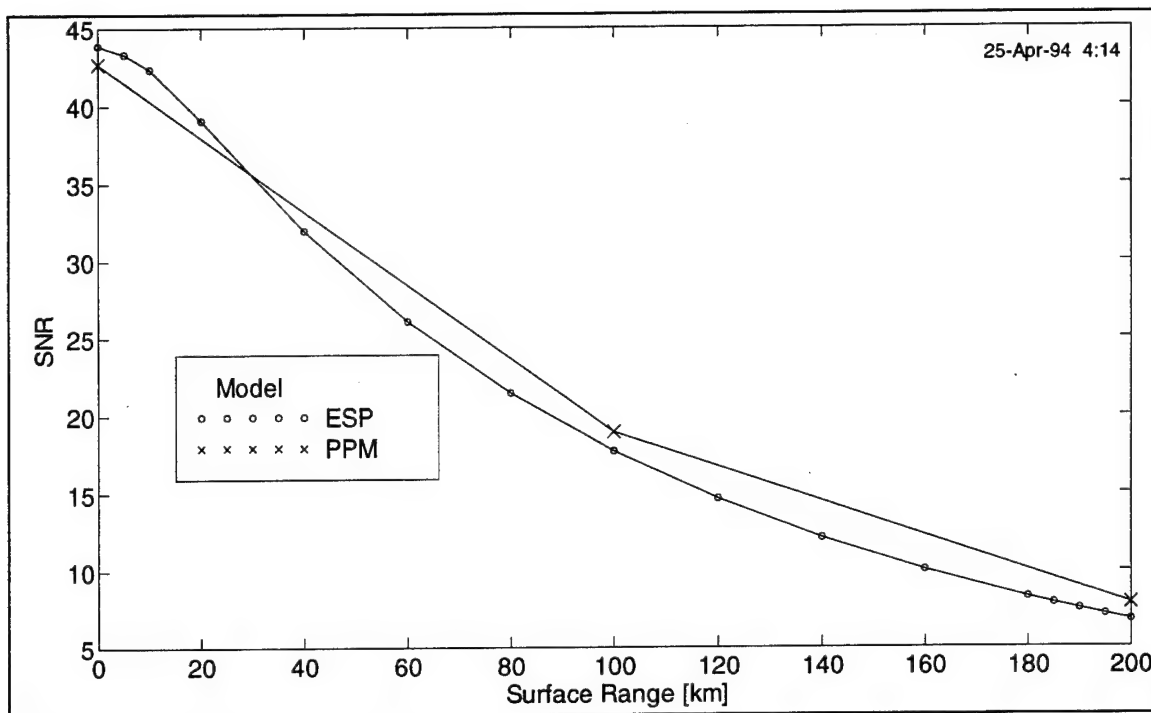


Figure 2-15: SNR Comparison for MWIR Band, 23 km Met Range

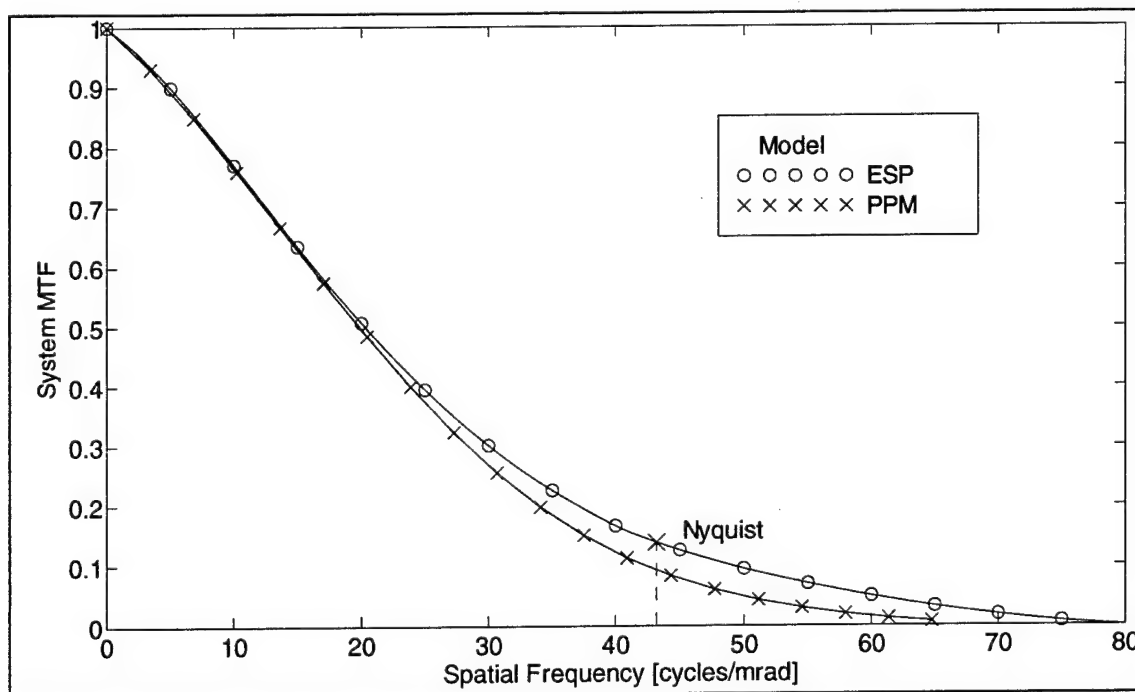


Figure 2-16. MTF Comparison for MWIR Band, 23 km Met Range

2.4.3 Minimum Detectable Temperature Difference (MDT) and Ground Resolved Distance

Since SNR and MTF results are very similar between the two models, performance predictors such as MDT (which are based on SNR and system MTF) can be expected to be similar as well. Calculation of derivative performance measures such as MDT or GRD were not conducted.

2.5 SENSOR COVERAGE CONSIDERATIONS

The PPM calculates coverage for a given IIRS value at the mid point (in angle) of the swath [see Figure 2-17]. Once the far point surface range has been determined, the PPM model can be run a second time at that range to determine the IIRS value at the far end of the swath. The ESP model has adopted coverage calculations where the desired minimum IIRS is specified at the distant end of the swath. Given that the two models yield similar results for IIRS as a function of surface range (excepting the long ranges discussed above), similar coverage results can be expected. Since comparisons between the two models would indicate nothing more than agreement on the calculation of the time available for a cross scan (and thus the scan width on the ground), no coverage calculations were performed.

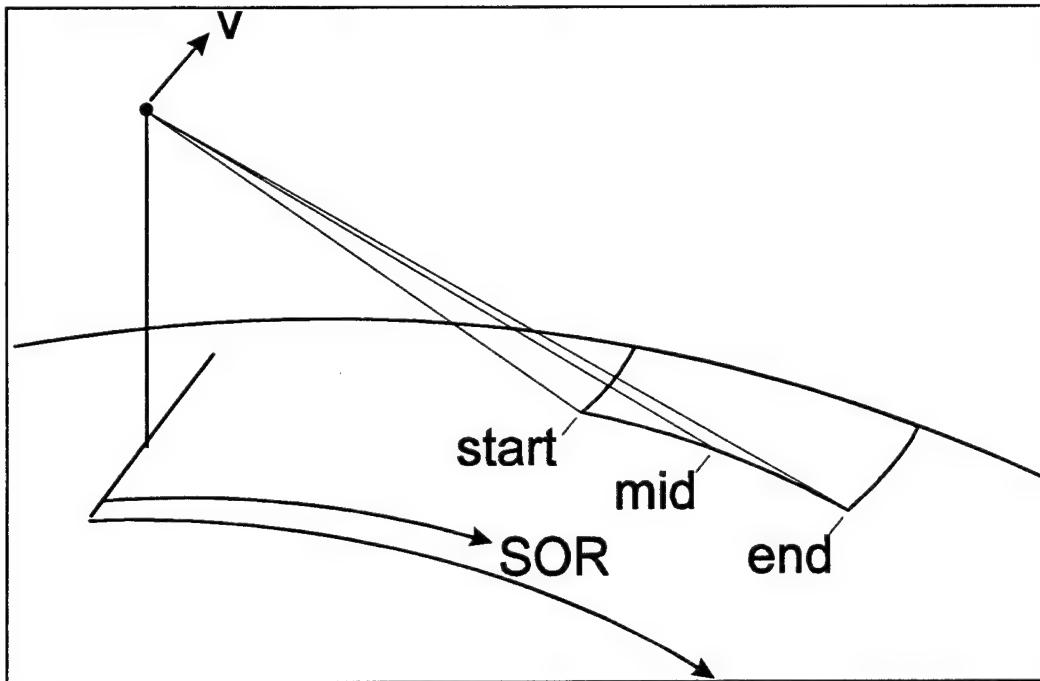


Figure 2-17: Coverage Swath Definitions

2.6 SUMMARY

Both the PPM and ESP models yield consistent results for SNR, system MTF, and GRD predictions. Remarkably similar results are obtained for the IIRS image quality predictions, since the methodologies to obtain IIRS used by the two modeling codes are different. It is suspected that the coefficient for the SNR term used in the PPM is much too small, since a factor of two increase in GRD at long surface range (and low SNR) is not reflected in a decrease in predicted IIRS. Since the PPM IQE is similar in form to that used by the image exploitation community, this equation is the preferred equation to use; the IQE coefficients must first be reviewed and updated as necessary.

Although very detailed in its treatment of the F sensor, the PPM is tailored to the whiskbroom sensor and would require considerable effort to modify for sensors which depart significantly from the F sensor. Considerable knowledge and facility with MathCad and Excel Macro worksheets and their interactions must be mastered before modifications can be made by the user.

3.0 MBS STABILITY ANALYSIS AND MODELING

3.1 INTRODUCTION

This report culminates the modeling and analysis development of the MBS magnetic controller. The work is based on information received from the program office. This task used MathCAD 5 Plus and Excel 5.0 for its development environment.

The MBS is represented in Figure 3-1 by nine components. Seven of the components are analog control, one is digital, and the other is the mass (J) of the device under control. Of the seven analog, three are electromagnetic actuators, a torque motor, and 3 sets of feedback sensors. The actuators are theoretically identical. They can be represented by a simple free body diagram. In the real physical system each actuator has two degrees of freedom. Each degree is represented by an independent circuit. The actuator model described in this paper is a generic representation of the theoretical system that is the basis for the six electromagnets designed into the MBS. The sensors shown in Figure 3-1 serve as feedback for actuator control and thus are part of the circuit modeled.

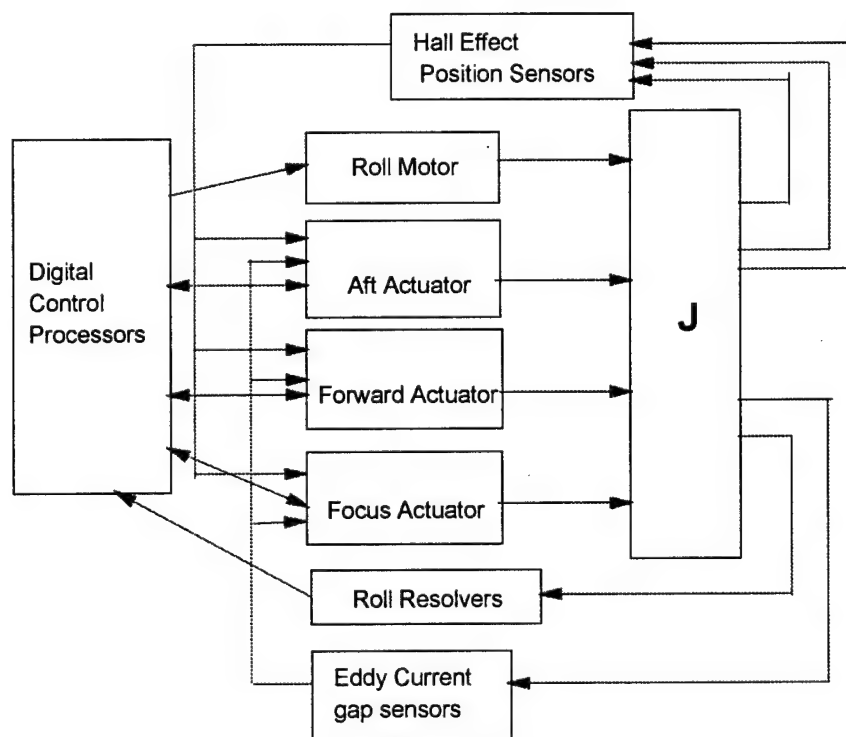


Figure 3-1: MBS Control Components

3.2 LIST OF REFERENCE OR APPLICABLE DOCUMENTS

The following is a list of the documents received from the program office. The work presented in this report is extensively based on the information contained in these documents. With the exception of the drawings listed, the documents fall into two informational categories. They are either design requirements/specification or theoretical modeling type of documents. The mechanical drawings are dimensionless pictures of the MBS structure. None of the documents represent real tested characteristics of the MBS.

1. Critical Design Review (CDR), Magnetic Bearing Subsystem, dated 23 April 1993.
Received 19 July 1993.
2. Action items for 21 July Mag Bearing CDR. Received 28 July 1993.
3. SatCon company brochure. Received 19 July 1993.
4. MBS CDR Controller Design, dated 7 April 1993. Received 19 July 1993.
5. Magnetic Bearing Subsystem (MBS), Controller Presentation, received 21 July 1993.
6. Magnetic Bearing Subsystem (MBS) Program Management Review, dated 18 February 1993.
7. Magnetic Bearing Subsystem (MBS) Electronics, Critical Design Review, dated 21 July 1993.
8. Set of 9 electrical schematics "Red" stamp dated 20 July 1993, received 21 July 1993.
Drawings on file are:
 - Drawing # (Dwg#), 1072904 (1/2 & 2/2)
 - Dwg# 1072907
 - Dwg# 1072905
 - Dwg# 1072909
 - Dwg# 1072908
 - Dwg# 1072903
 - Dwg# 1072901
 - Dwg# 1072910 (1/2 only).
9. Memorandum, Response to S-100 MBS Questions of 3 December 1993.
10. Response to MBS Questions of 16 Feb. 94, Memorandum # 9770-94-075.
11. MBS Control Modeling III, Memorandum # 9770-94-067.
12. Appendix to Memorandum # 9770-94-075.
13. Test and Evaluation Master Plan (TEMP), for the MBS.
14. Documentation Tree.
15. ES264834: MBS Engineering specification.
16. Example of Modulation Transfer Function MathCAD Template (Sanitized).
17. Software TIM, MBS Software Review 4/6/94.
18. CIDS for MBS Control Algorithms Spec. # C172104.
19. SDRL No. S013, Soft. Requirements Spec. for the MBS-Controller CSCI date 2/17/94.
20. SDRL No. S022 Soft. Req. Spec. for the MBS-Controller CSCI.
21. SDRL No. S025, Rev B, Soft. Req. Spec. for the MBS-Controller CSCI.
22. SLOC 2-17-94, Language: ADA, source code listing of 6 ADA files.
23. ES261468, Interface Control Document for the MBS.
24. Roll Gimbal with Laser Gyro & FSM Control Loop Response; simulation source code.

25. Combined Vertical/Lateral Actuator Model Forward Actuator; simulation source code.
26. Combined Vertical/Lateral Actuator Model Aft Actuator; simulation source code.
27. Actuator Model Equations.
28. Results of Error Sensitivity Simulations; Excel spread sheet tables.
29. Dwg. #42294A, Rec. 4/22/94; 3D line drawing with no name or number of the Stator Assembly.
30. Dwg. #1072488, Rotor Assembly Final Grind.
31. Dwg. #1072490 Front Plate-Roll Motor Assembly; 2 sheets.
32. Dwg. #42294B, Rec. 4/22/94; 3D line drawing showing stator with fairly good view of the caging mechanism.
33. Dwg. #1072493, Rotor Assembly- Bonding; 2 sheets.
34. Dwg. #1072501, Core & Pole Assy FWD Support Actuator.
35. Dwg. #1072507, Core & Coil Assy AFT Support Actuator; 2 sheets.
36. Dwg. #1072516, Pole & Core Assembly Focus AFT Pulling.
37. Dwg. #1072517, Pole & Core Assembly Focus, Forward Pulling.

3.3 TECHNICAL DISCUSSION

Based on the information obtained from the references, the modeling was primarily done in the frequency domain with some work done in the time domain . The methods of analysis were interpretation of Nyquist contour plots and constant M-Circles. The Nyquist plots were used to demonstrate that the controller could be stable within a range of coefficients. The constant M-Circles were used to show that the system could have sufficient bandwidth to meet requirements as stated in references #15 and #23.

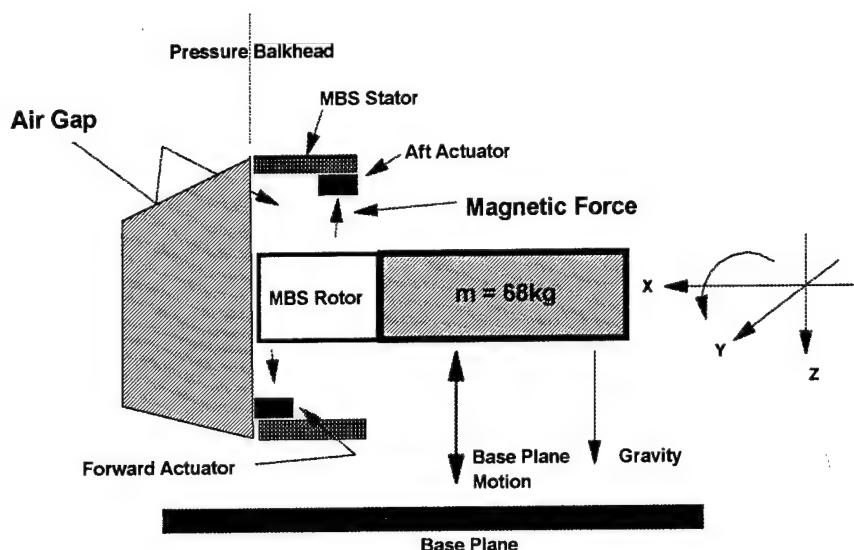
Figure 3-2 is an over-simplified free body diagram of the MBS structure. Its intent is to show the cantilever configuration and the general direction of the magnetic forces generated by the actuators. The focus actuators are not shown. Their design is a scaled version of the Forward and Aft actuators.

The type of modeling presented is Input/ Output (I/O), with Nyquist plots and constant M-Circles. This method looks at a system's transfer function and determines the number of poles and zeroes. From this a graphical plot (picture), is made that can be used to comment on the relative stability of the function. I/O models assume that all initial conditions are zero and they can be generated analytically or empirically. In this analysis all plots were analytical.

The magnetic actuator's transfer functions, modeled $G_{eq}(s)$, were derived from reference #'s 4, 7, 11, 15 and 23. The forward vertical/lateral, aft vertical/lateral and focus actuators use the same form of $G_{eq}(s)$. To model a specific actuator a profile is built containing the coefficients unique to the physical device. For example, the forward actuator has 11 poles, aft has 19 and focus has 5.

From the models and respective charts presented, it can be seen that the transfer functions for the actuators are stable for a wide selection of gain and coefficients. This does not

take into account any disturbance on these systems from the base plane source. But it does show that they can be very stable.



Free Body Diagram

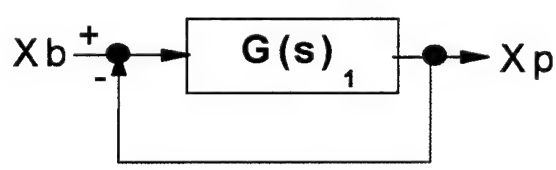
Figure 3-2: Free Body Diagram of MBS Structure

The MBS is put in operation from the caged mode. In the caged mode, the MBS is caged with the nominal gap of 3.1mm. Prior to releasing the caged device, the actuators are powered to the level required to suspend the rotor at the nominal gap (set point). The nominal gap is a set point generated by a command from the MBS software. With this scheme, the actuators are not required to raise the rotor from the safety supports. This may reflect a power savings. Not having to do this could lower the duty cycle requirements on the power subsystem. In addition being able to cage to the nominal set point could widen the area of controllability. This could become a critical point. We have a linear controller operating on a nonlinear phenomenon in a vibration environment described by a set of PSDs (ref. #15). As seen by Eq.2 of the MathCAD templates (Appendix A), the magnetic force applied to the rotor is nonlinear with respect to both gap (Gap), and controller output current (I). Meeting the settling, slew and collision requirements could be challenging.

This modeling is useful in helping to plan, develop or refine the MBS testing program. As real test data is published on the current device, it can be input into the model for correlation. As it becomes necessary to characterize the detailed effects of disturbances on the MBS, Root Locus and state space representation models could be investigated. With the addition of a complete state space model the MBS as a system would be fully characterized. This would

enable the modeler to investigate a whole range of possible design configurations as the MBS BOM settles into steady state.

Figures 3-3 and 3-4 show the block diagrams of transfer functions $G_{eq}(s)$ and $G_{tot}(s)$, respectively. The component transfer functions are defined in the attached MathCAD templates. Nyquist contour plots were developed for each. The parameters that form the coefficients are the best representation of the theoretical system at this moment. As the latest design documentation becomes available, the model could be updated.

$$G(s)_{eq} = \frac{G_p G_f G_a G_J}{1 + G_f G_a - G_a G_J H_g}$$


$$\frac{X_p}{X_b} = \frac{G(s)_{eq}}{1 + G(s)_{eq} H} \quad H = 1$$

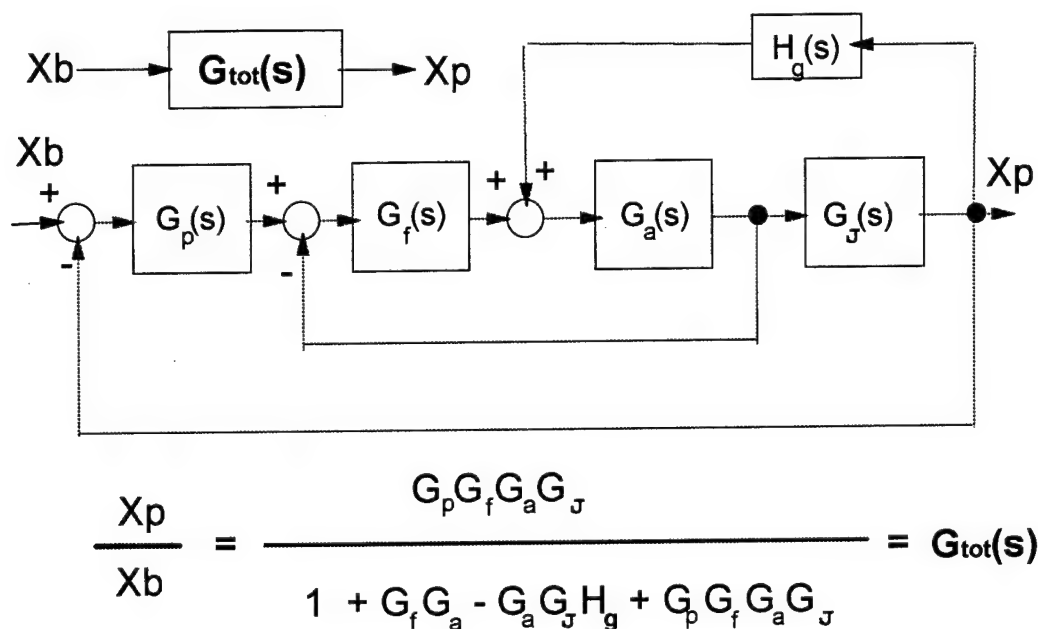
Actuator Control System

Figure 3-3: Actuator Control System Block Diagram

The Roll Torque motor is modeled as a second order system with the resolver as negative feedback. The motor has three windings that are independently controlled. Modeled are two variations of the motor. One with variable armature current and the other with variable field current. The actual MBS torque motor is a DC brush less motor. Motors of this type are sometimes referred to as "pancake" motors. At this time not much is known about the real characteristics of this motor. All that has been mentioned (verbally), is that it will deliver the torque as commanded by the SCP. For modeling proposes this would be a torque command in, with a torque out linear relationship.

The torque motors modeled are typical of the characteristics of a wide range of off-the-shelf motors. The MathCAD templates for typical torque motors is attached to this report. The MBS motor is a design specific to the MBS using mature DC brush less technology. The developers have reported that their initial testing of the motor has gone well. They have tested it

on both a bread board and MBS assemblies with realistic loads. These test were done with zero base plane vibration.



Actuator Control System

Figure 3-4: Actuator Control System Block Diagram

3.4 CONCLUSION

The MBS design has evolved significantly in the past year. Much still needs to be done. There is currently a prototype built. It will need to undergo laboratory testing, debugging and modification over the next year. From a stability point of view, more than likely its main challenge will be in the design of the flux and position compensators. These devices reside in the inner and outer control loops of the hardware controller. Without them the MBS would not be stable. As the MBS is tested to verify its compliance with the vibration requirements it is likely that these devices could be in the critical path. As the MBS's response to real loads is determined, the compensators may need adjusting to tune into the precise pole location.

It is recommended that the Air Force continue with its modeling or simulation studies. Through these studies tremendous insight of the characteristics of the acquisitioned technology can be independently gained. Having this capability within the Program Office would aid the scheduling and budgeting processes as well as assist in the application of the technology.

4.0 REFERENCES

1. "Image Interpretability Rating Scale," Air Standard Coordinating Committee, Air Standard 101/103, Annex A.
2. *Exploratory Advanced Development Model, Performance Prediction Model (PPM) Report*, CDRL Sequence No. A026, Contract No. 7403.

APPENDIX
MBS MATHCAD TEMPLATES

Generic Actuator Controller Model

This model can be set up to model either the Forward, Aft or Focus Actuators. By varying the coefficients on the numbered equations, the stability characteristics of an actuator can be studied.

The following variables are for the definition of the graphics.

$n := 0..100$	Number of points to be plotted.
$d := 1 \quad r := 1$	Radius of small arc.
$c := 0 \quad m := 0..400$	Pole to encircled and size of matrix.
$t_n := .01 \cdot n$	Weighted value to scale plot.
$RR := 100$	Radius of big arc.

The following equation are used for plotting the contours of the transfer functions. They define the graphics in the complex plane.

$L(t, x, y, z) := z \cdot j + x \cdot j + t \cdot (y - x) \cdot j$	These equations draw the Nyquist contours.
$A(t, e, r, d) := e \cdot j + r \cdot \exp(j \cdot (.5 - t) \cdot d \cdot \pi)$	L is for the vertical line and A is for the two arcs.

$P_n := L(t_n, r, RR, c)$	$P_{n+100} := A(t_n, c, RR, 1)$	These equations calculate the matrix of points to be plotted.
$P_{n+200} := L(t_n, -RR, -r, c)$	$P_{n+300} := A(t_n, c, r, -1)$	

The following variables are for the definition of the electromagnetic circuit. These were initially taken from S122 source code back in October 93. See reference document #12. Since then they have been varied to study the sensitivity of each to the stability of the controller.

$Lm := 0$	$R := 100$	$inch := 0.0254$	$Fo := 11.68$
$Np := 4$	$Old_R := 36.09$	$Ap := 1.0544 \cdot inch^2$	
$Nt := 780$	$\mu 0 := 4 \cdot \pi \cdot 10^{-7}$	$g0 := 3.1 \cdot 10^{-3}$	

The following equations were derived from reference document #'s 4, 11, 12 and 15.

$$L_o := \mu_0 \cdot A_p \cdot N_p \cdot \frac{N_t^2}{(L_m + g_0)} \quad \text{Equ.3}$$

$$R_{pp} := \frac{R}{(N_p \cdot N_t^2)} \quad \text{Equ.4}$$

Variables for the following equations.

$$l_m := .001 \quad B_r := 1 \quad \text{gap} := .00498 \quad i := 5$$

$$B := \frac{B_r \cdot l_m}{(l_m + \text{gap})} + \frac{i \cdot \mu_0 \cdot N_t}{(l_m + \text{gap})} \quad \text{Equ. 5}$$

$$K_v := \frac{1}{(A_p \cdot N_p \cdot N_t)} \quad \text{Equ. 6 compensator gain constant.}$$

$$B = 0.987 \quad \text{calculated value}$$

$$K_g := -\frac{R_{pp} \cdot B}{(\mu_0 \cdot A_p)} \quad \text{Equ7, Feedback constant.}$$

$$B_0 := \sqrt{\frac{2 \cdot F_o \cdot \mu_0}{(A_p \cdot N_p)}} \quad \text{Equ8.}$$

$$B_0 = 0.104 \quad \text{Calculated value.}$$

$$K_b := \frac{A_p \cdot B \cdot N_p}{\mu_0} \quad \text{Equ9.}$$

$$K_b = 2.137 \cdot 10^3 \quad \text{Calculated value.}$$

$$KK_b := 2 \cdot F_0 \quad \text{Equ10}$$

$$KK_b = 23.36 \quad \text{Calculated value.}$$

$$M_a := 68. \quad \text{Supported cantilevered weight.}$$

Position Compensator

$$G_p(s) := \frac{(s + .6285436744788757886) \cdot (s + 3.769790402570060698)}{s \cdot (s + 125.7)} \quad \text{Equ11.}$$

Flux Compensator

$$G_f(s) := \frac{(s + 157.05765407554671968) \cdot K_v}{s \cdot (s + 31420.)} \quad \text{Equ12.}$$

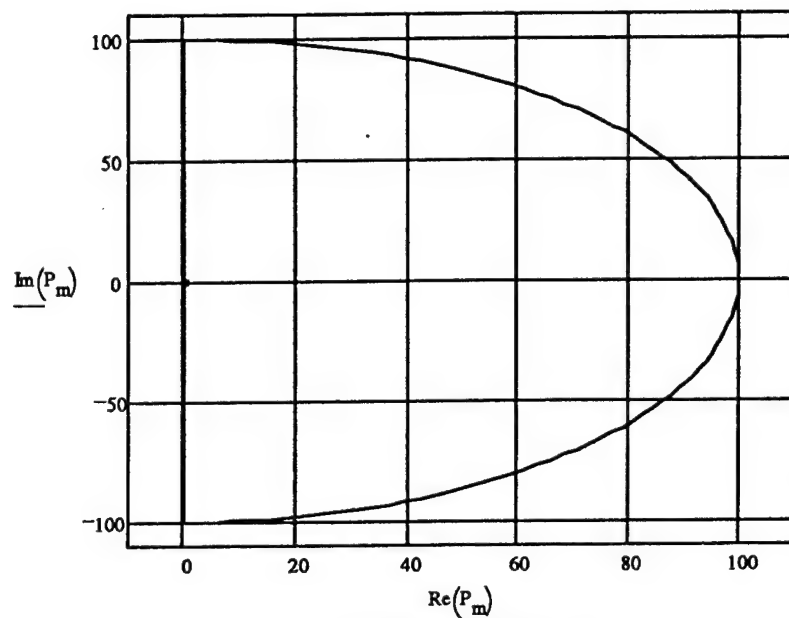
Actuator Coil & Supported Mass

$$G_a(s) := \frac{1}{\left(s + \frac{R}{L_0}\right)} \cdot \left(\frac{K_b}{M_a \cdot s^2}\right) \quad \text{Equ13.}$$

$$G(s) := \frac{1}{\left(s + \frac{R}{L_0}\right)} \cdot \left(\frac{K_b}{M_a \cdot s^2}\right) \cdot G_p(s) \cdot G_f(s) \quad \text{Equ14.}$$

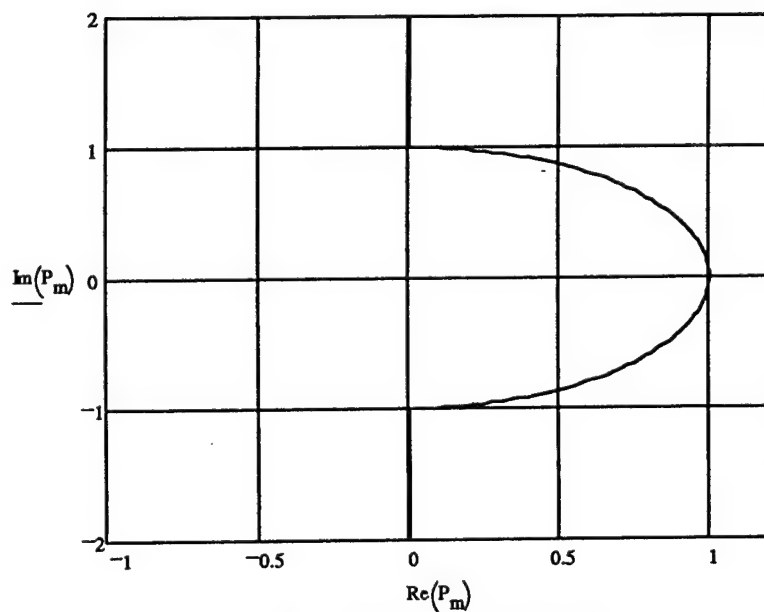
These Plots are of $P(s)$ in the complex plane. They are examples of typical Nyquist plots. They are drawn here to verify that the graphics are functioning properly.

Generic Nyquist Contour Plots in the complex plane.



Verification Plot, Fig. 1

Magnification of contour plot at the origin.



Magnification at Origin, Fig. 2

Total plot showing clockwise encirclement.

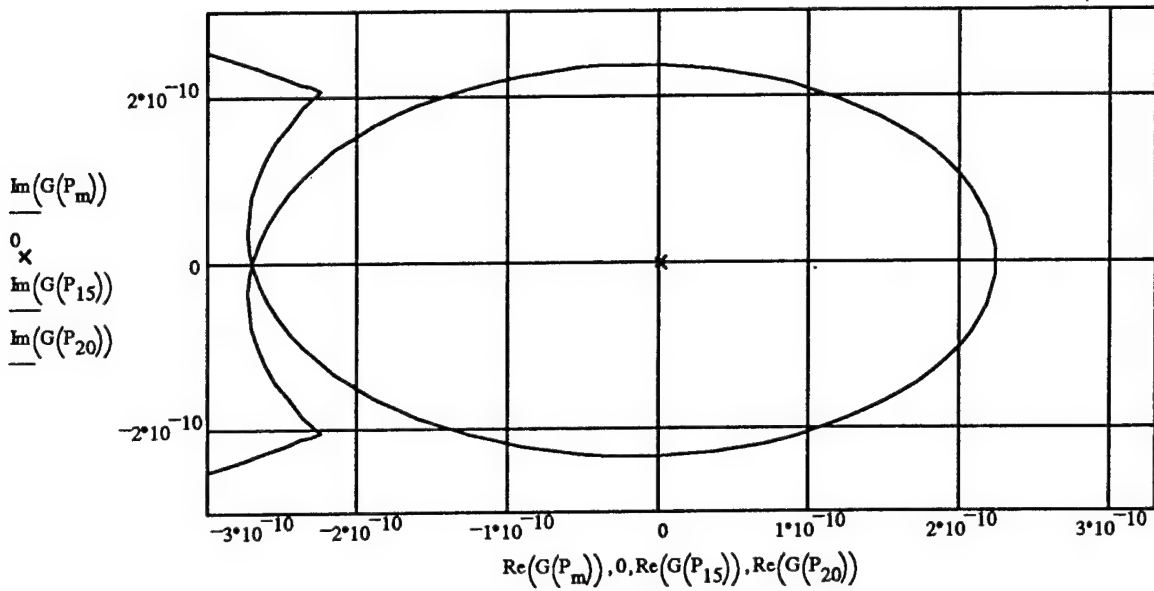


Fig. 3

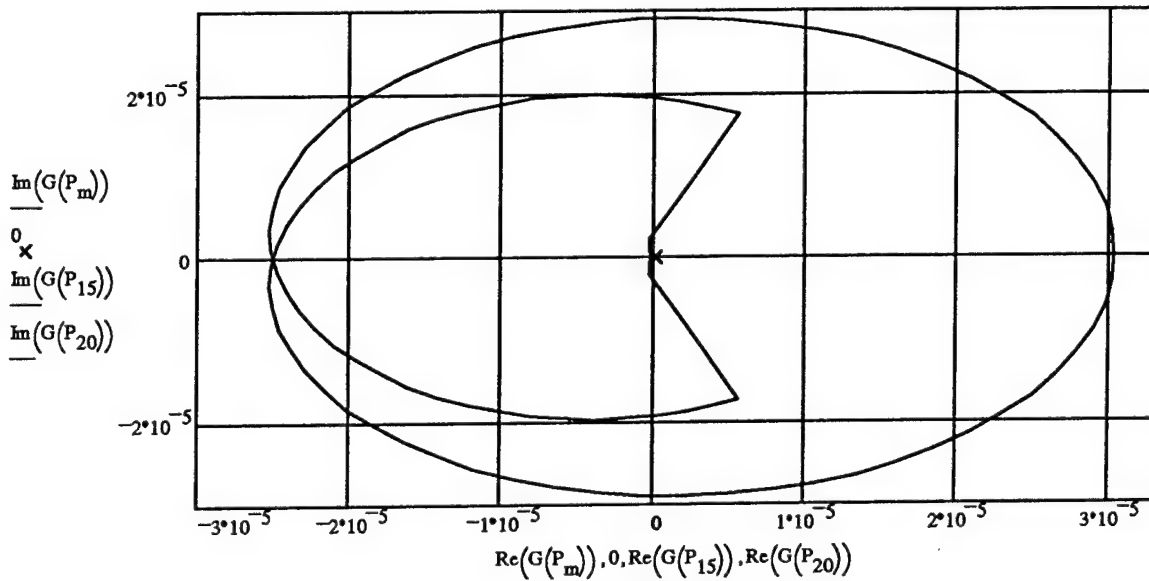


Fig. 4

$$G_{fa}(s) := G_f(s) \cdot G_a(s)$$

$$G_{ag}(s) := G(s) \cdot K_g$$

Geq Representation with unity feedback.

$$G_{eq}(s) := \frac{G(s) \cdot 10^4}{(1 + G_{fa}(s) - G_{ag}(s) + G(s))}$$

Equ.15

Contour plot of an actuator control circuit.

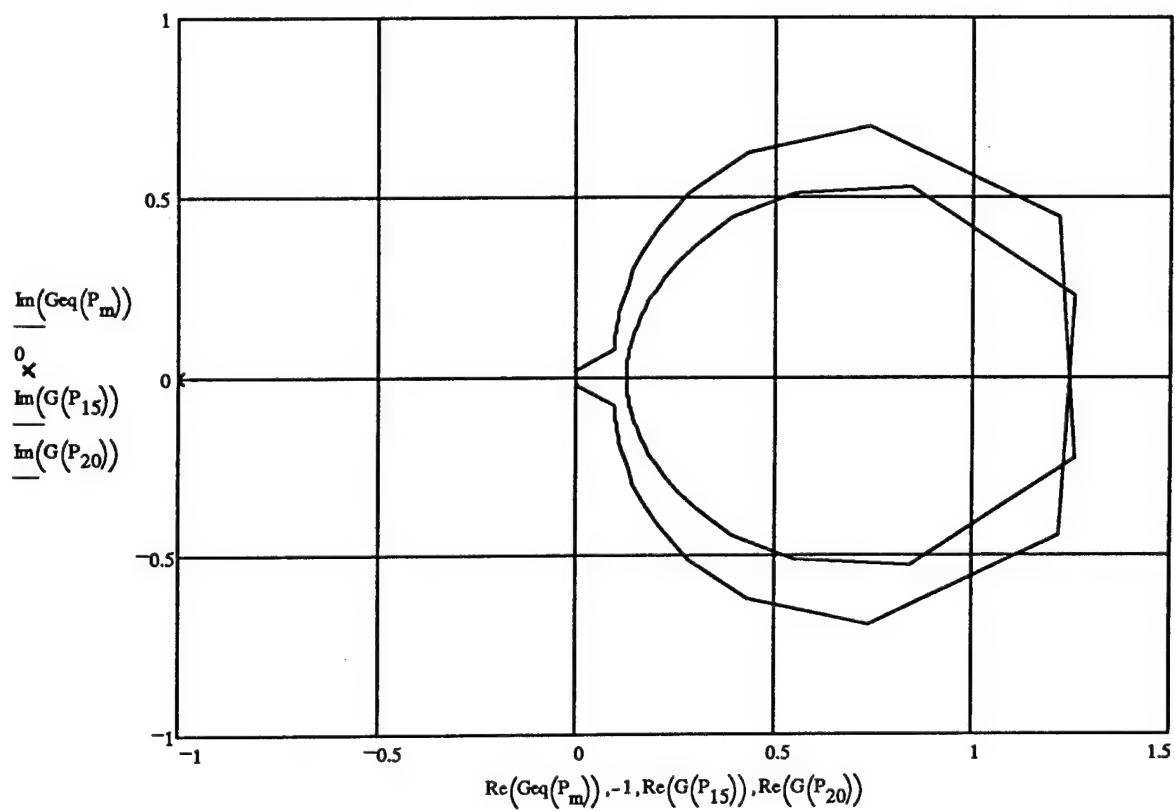


Fig. 5

The following is the graphical definition of the Constant M-Circles.

$$10 \cdot n + .001 \text{ mm} := 0..100$$

$$10^{.02 \cdot n} \quad M := 2.05$$

$$C(\text{mm}) := \left(\frac{-M^2}{M^2 - 1} + \left| \frac{M}{M^2 - 1} \right| \cdot \exp(2 \cdot \pi \cdot j \cdot -.01 \cdot \text{mm}) \right)$$

Equation 16, is the Transfer function plotted for the M-Circle.

$$n := 0..100$$

$$\omega(n) := 10 \cdot n + .001$$

$$\text{Geqq}(s) := \frac{G(s) \cdot 10^9}{(1 + Gfa(s) - Gag(s))} \quad \text{Equ.16}$$

Plot indicating bandwidth of Geq, 'Constant M-circle'.

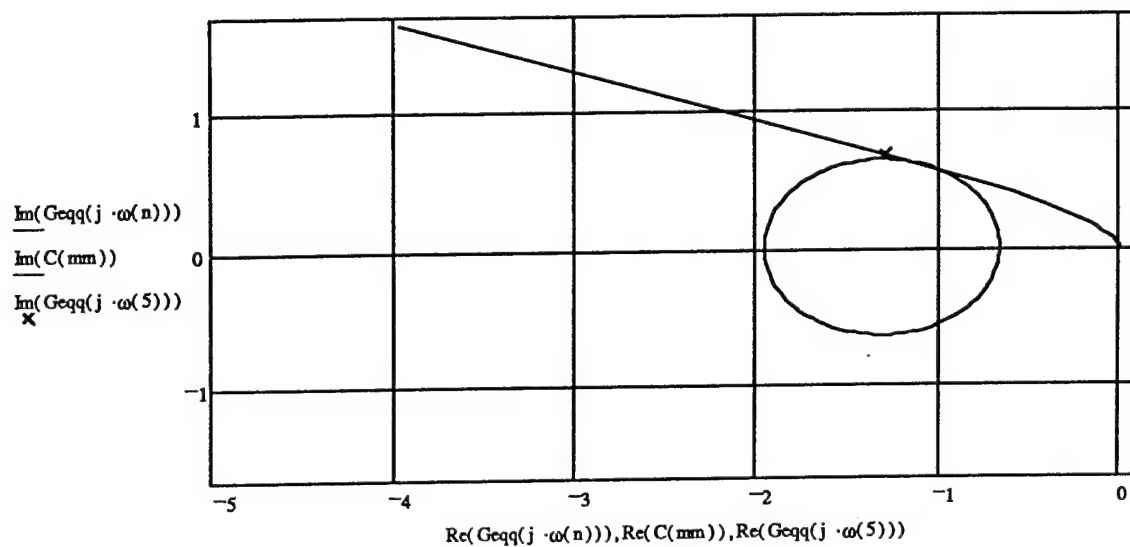


Fig. 6

Math Model of MBS Roll Torque Motors

The motors modeled here are DC armature and field current controlled motors. Values for the selected coefficients are typical of those for off the shelf motors. The load is the MBS specification.

The following variables define the graphics required to plot in the complex plane.

$R := 100$	This is the outer radius of the contour plot.
$n := 0..100$	This defines the numbe of points to be generated during the plotting.
$c := 0$	This defines the complex point to circle.
$d := 1$	This defines the diameter of the small graphic circle.
$r := 1$	This defines the inner radius of the countour plot.
$m := 0..400$	This defines the size of the array to be plotted.
$t_n := .01 \cdot n$	This defines a weighting factor for the plot.

The following two equations are for the drawing of the vertical and arc lines of the Nyquist contour plot. They are the same as those shown on page1.

$$L(t, x, y, z) := z \cdot j + x \cdot j + t \cdot (y - x) \cdot j \quad A(t, e, r, d) := e \cdot j + r \cdot \exp(j \cdot (.5 - t) \cdot d \cdot \pi)$$

$$P_n := L(t_n, r, R, c) \quad P_{n+100} := A(t_n, c, R, 1)$$

$$P_{n+200} := L(t_n, -R, -r, c) \quad P_{n+300} := A(t_n, c, r, -1)$$

The following coefficients and equations define the Armature controlled motor.

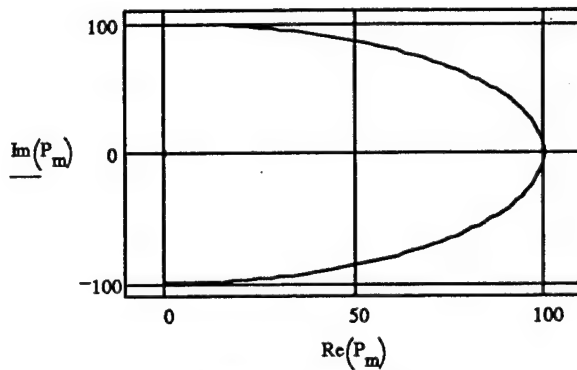
$m_a := 68.$	Mass of unit load in Kg., from the MBS specification.
$r_o := .50$	Moment arm.
$\beta := .01$	Viscous damping coefficient.
$T_q := 10$	Specified Torque.
$K_v := .1$	Back emf constant.
$R_a := 40$	Armature resistance
$I_a := 2$	Armature current.
$J := 0.5 \cdot m_a \cdot r_o^2$	Mass moment.
$L_a := 4.7 \cdot 10^{-3}$	Armature inductance in henry's
$J = 8.5$	Calculated value.
$K_t := \frac{T_q}{I_a}$	Torque constant.
$K := 5.0$	Arbitrary gain used for investigations.
$\frac{\beta}{J} = 0.001$	Coefficient calculated value
$\frac{R_a}{L_a} = 8.511 \cdot 10^3$	Coefficient calculated value
$\frac{K_t}{J \cdot L_a} = 125.156$	Coefficient calculated value

Expression for an armature controlled DC motor.

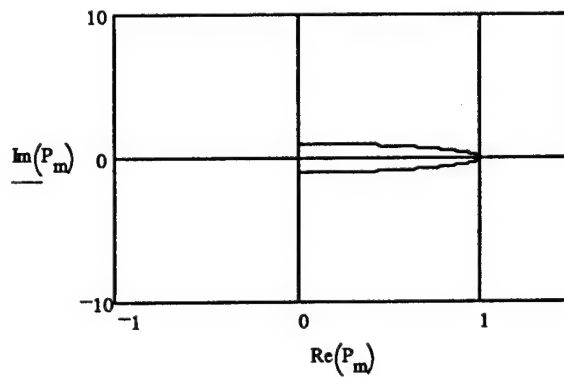
$$s^3 + \left(\frac{\beta}{J} + \frac{R_a}{L_a}\right) \cdot s^2 + \left(\frac{\beta \cdot R_a}{J \cdot L_a} + \frac{K_t \cdot K_v}{J \cdot L_a}\right) \cdot s - \frac{K_t}{J \cdot L_a} + \frac{K_t}{J L_a} \quad \text{Equ. 17}$$

The following plots verify the setup for the graphics.

Nyquist Contour



Complete Generic Contour Fig 7



Magified Origin, fig. 8

I/O expression for the motor.

$$\left[s^3 + \left(\frac{\beta}{J} + \frac{Ra}{La} \right) \cdot s^2 + \left(\frac{\beta \cdot Ra}{J \cdot La} + \frac{Kt \cdot Kv}{J \cdot La} \right) \cdot s \right] - \frac{Kt}{J \cdot La} \quad \text{Equ. 18}$$

Armature Controlled Motor Transfer Function with gain K and mass moment J..

$$Gp(s) := \frac{K \cdot \frac{Kt}{J \cdot La}}{\left[s^3 + \left(\frac{\beta}{J} + \frac{Ra}{La} \right) \cdot s^2 + \left(\frac{\beta \cdot Ra}{J \cdot La} + \frac{Kt \cdot Kv}{J \cdot La} \right) \cdot s \right] - \frac{Kt}{J \cdot La}} \quad \text{Equ. 19}$$

The gain K, was inserted to aid in the analysis of this type of motor.

Figures 9 and 10 show that a motor of this type with the a given set of coefficients can be stable. This is not a surprise conclusion. Motors of this type have been built for years. The reason for this model is to faciliate the investigation of the MBS motor when its coefficients are published.

Nyquist Plot of Motor Transfer function

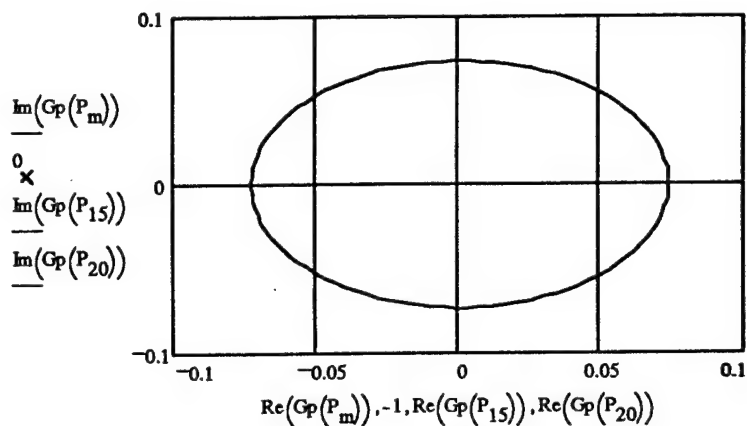


Fig. 9

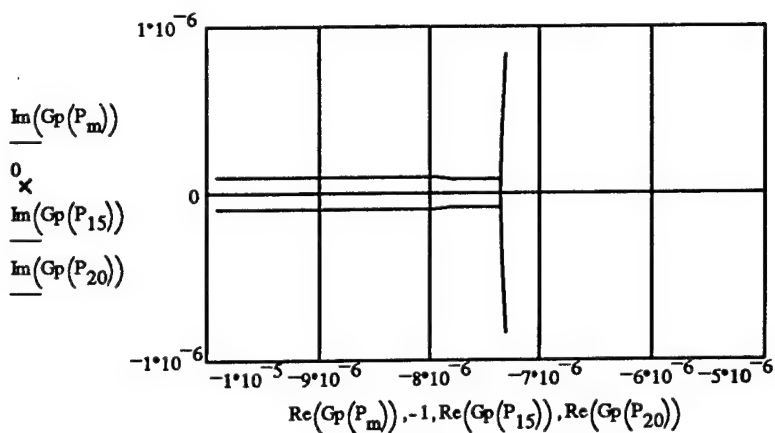


Fig. 10

The following coefficients and equations define the Field controlled motor.

$L_f := 4.7 \cdot 10^{-3}$ Field inductance in henry's.

$R_f := 40$ Field resistance in ohms.

$I_f := 2$ Field current in amps.

$J = 8.5$ Calculated mass moment.

$K := 5.0$ Gain factor.

$$K_t := \frac{T_q}{I_f}$$

$$\frac{R_f}{L_f} = 8.511 \cdot 10^3$$

Calculated Coefficients

$$\frac{\beta}{J} = 0.001$$

$$\frac{K_t}{J \cdot L_f} = 125.156$$

Field Controlled Motor Transfer function.

$$G_{pf}(s) := \frac{K \cdot \frac{K_t}{J \cdot L_f}}{s \cdot \left(s + \frac{\beta}{J}\right) \cdot \left(s + \frac{R_f}{L_f}\right)} \quad \text{Equ. 20}$$

Figures 11 and 12 are the typical plot of a stable Field controlled motor.

Nyquist Plot of Motor Transfer function

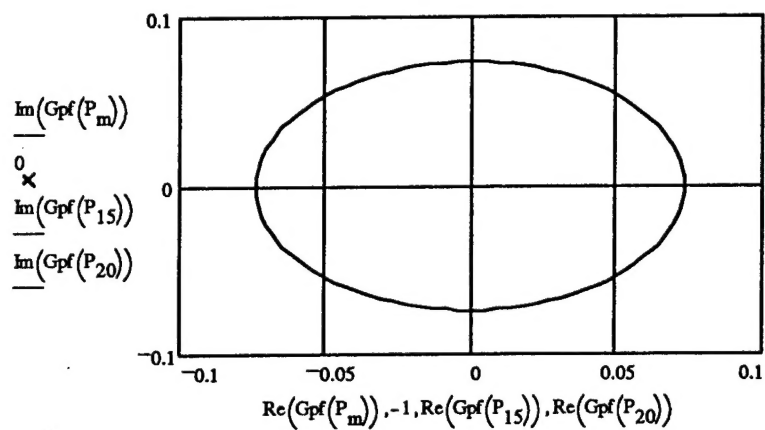


Fig. 11

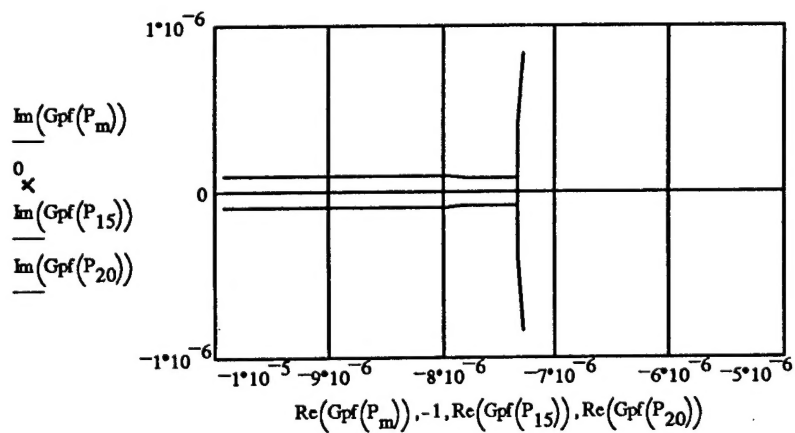


Fig. 12

Model of Magnetic Actuator Force

Parameter values taken from references #4 & #5.

$N_t := 780$	Number of turns in a couil
$\mu_o := (4.0 \cdot \pi \cdot 1 \cdot 10^{-7})$	Permeability of gap
$A_p := 680.0$	Area of coil in 'mm ²
$N_p := 4$	Number of poles
$Gap := 3.1$	Distance between rotot and stator in 'mm'.
$I := 0, .1 .. 2.0$	Actuator driver current in terms of Amps.
$I_o := 0.325$	Bias current in Amps.

$$B(I) := \frac{N_t \cdot I \cdot \mu_o}{Gap} \quad \text{Equ. 21} \quad \text{Equation for magnetic flus density.}$$

$$F(B) := \frac{B(I)^2 \cdot A_p \cdot N_p}{(2 \cdot \mu_o)} \quad \text{Equ. 22} \quad \text{Equation for the force created by a magnetic feild.}$$

Or if we substitute equation Eq.21 into Eq.22.

$$F(I, Gap) := \left(\frac{N_t \cdot A_p \cdot N_p \cdot \mu_o}{2} \right) \cdot \frac{I^2}{Gap^2} \quad \text{Equ. 23}$$

Figure 13 shows the non linear characteristics of the force function with respect to the drive current at the nominal gap.

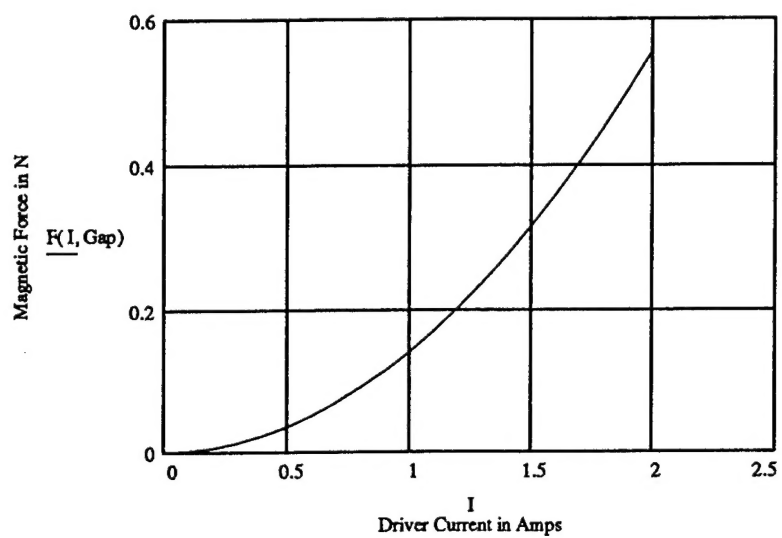


Fig. 13